



2013-12-13

# Effect of Full-Annular Pressure Pulses on Axial Turbine Performance

Mark H. Fernelius

*Brigham Young University - Provo*

Follow this and additional works at: <https://scholarsarchive.byu.edu/etd>



Part of the [Mechanical Engineering Commons](#)

---

## BYU ScholarsArchive Citation

Fernelius, Mark H., "Effect of Full-Annular Pressure Pulses on Axial Turbine Performance" (2013). *All Theses and Dissertations*. 3825.  
<https://scholarsarchive.byu.edu/etd/3825>

This Thesis is brought to you for free and open access by BYU ScholarsArchive. It has been accepted for inclusion in All Theses and Dissertations by an authorized administrator of BYU ScholarsArchive. For more information, please contact [scholarsarchive@byu.edu](mailto:scholarsarchive@byu.edu), [ellen\\_amatangelo@byu.edu](mailto:ellen_amatangelo@byu.edu).

Effect of Full-Annular Pressure Pulses on Axial Turbine Performance

Mark H. Fernelius

A thesis submitted to the faculty of  
Brigham Young University  
in partial fulfillment of the requirements for the degree of  
Master of Science

Steven E. Gorrell, Chair  
Dale R. Tree  
Tadd T. Truscott

Department of Mechanical Engineering  
Brigham Young University  
December 2013

Copyright © 2013 Mark H. Fernelius  
All Rights Reserved

## ABSTRACT

### Effect of Full-Annular Pressure Pulses on Axial Turbine Performance

Mark H. Fernelius  
Department of Mechanical Engineering, BYU  
Master of Science

Pulse detonation engines show potential to increase the efficiency of conventional gas turbine engines if used in place of the steady combustor. However, since the interaction of pressure pulses with the turbine is not yet well understood, a rig was built to compare steady flow with pulsing flow. Compressed air is used in place of combustion gases and pressure pulses are created by rotating a ball valve with a motor. This work accomplishes two main objectives that are different from previous research in this area. First, steady flow through an axial turbine is compared with full annular pulsed flow closely coupled with the turbine. Second, the error in turbine efficiency is approximately half the error of previous research comparing steady and pulsed flow through an axial turbine. The data shows that a turbine driven by full annular pressure pulses has operation curves that are similar in shape to steady state operation curves, but with a decrease in turbine performance that is dependent on pulsing frequency.

It is demonstrated that the turbine pressure ratio increases with pulsed flow through the turbine and that this increase is less for higher pulsing frequencies. For 10 Hz operation the turbine pressure ratio increases by 0.14, for 20 Hz it increases by 0.12, and for 40 Hz it increases by 0.06. It is demonstrated that the peak turbine efficiency is lower for pulsed flow when compared with steady flow. The difference between steady and pulsed flow peak efficiency is less severe at higher pulsing frequencies. For 40 Hz operation the turbine efficiency decreases by 5 efficiency points, for 20 Hz it decreases by 9 points, and for 10 Hz it decreases by 11 points. It is demonstrated that the specific power at a given pressure ratio for pulsed flow is lower than that of steady flow and that the decrease in specific power is lower for higher pulsing frequencies. On average, the difference in specific power between steady and pulsed flow is 0.43 kJ/kg for 40 Hz, 1.40 kJ/kg for 20 Hz, and 1.91 kJ/kg for 10 Hz.

Keywords: pulsed flow, unsteady flow, axial turbine, turbine performance, pulse detonation, PDE

## ACKNOWLEDGMENTS

Funding for this project was provided by Innovative Scientific Solutions, Inc. and the Brigham Young University Department of Mechanical Engineering. I am grateful for the funding that these institutions provided that made this project possible.

I am appreciative of my advisor, Steven Gorrell, for the time he has spent working with me reviewing designs and working on papers. I am also grateful to my committee members, Dale Tree and Tadd Truscott.

I am grateful to Fred Schauer of the Air Force Research Laboratory and John Hoke of Innovative Scientific Solutions, Inc. for their input and work with the project.

Members of the Turbomachinery Research Laboratory have also been helpful throughout the project. Joshua Wilson assisted with much of the rig design and fabrication. Matthew Marshall helped me with a variety of computer issues and taught me how to use Adobe software to create more aesthetically pleasing figures. David Weston and Trevor Blanc gave suggestions and input that resulted in a better rig. I am grateful for all their help and input.

Gratitude is expressed to Jonathan Tellefsen for two of the drawings in Appendix A. Additionally, I am grateful to Steve Puterbaugh of the Air Force Research Laboratory for loaning the TSI Velocity Calibrator so that I could determine the thermocouple recovery factor.

I am also appreciative of the Mechanical Engineering Department staff. Specifically, Kevin Cole and Dave Laws for their technical advice, Ken Forster for his fabrication support, and Miriam Busch for helping me with university paperwork.

Finally, I am very grateful to my wife, Kaitlynn, for supporting me throughout my Master's and allowing me to spend many hours on campus studying and working on my project.

## TABLE OF CONTENTS

<b>LIST OF TABLES</b> . . . . .	<b>vi</b>
<b>LIST OF FIGURES</b> . . . . .	<b>vii</b>
<b>NOMENCLATURE</b> . . . . .	<b>ix</b>
<b>Chapter 1 Introduction</b> . . . . .	<b>1</b>
1.1 The Pulse Detonation Engine Cycle . . . . .	1
1.2 Disadvantages of Pulse Detonation Engines . . . . .	2
1.3 Advantages of Pulse Detonation Engines . . . . .	3
1.4 Objective . . . . .	4
<b>Chapter 2 Literature Review</b> . . . . .	<b>6</b>
2.1 PDE/GTE Integration Studies . . . . .	6
2.2 Averaging Methods . . . . .	10
<b>Chapter 3 Rig Design and Experimental Methods</b> . . . . .	<b>17</b>
3.1 JetCat Modification . . . . .	17
3.2 Rig Air Flow . . . . .	18
3.2.1 Bypass and Pulsing Valves . . . . .	19
3.2.2 Plenum and Inlet Manifold . . . . .	23
3.2.3 Compressor Air Flow . . . . .	26
3.2.4 Rig Air Flow Control Summary . . . . .	27
3.3 Instrumentation . . . . .	28
3.4 Turbine Lubrication and Alignment . . . . .	30
3.5 Testing Methodology . . . . .	32
3.6 Rig Modifications . . . . .	33
<b>Chapter 4 Results and Discussion</b> . . . . .	<b>35</b>
4.1 Error Analysis . . . . .	36
4.2 Repeatability Analysis . . . . .	39
4.3 Steady Flow Results . . . . .	39
4.4 Procedure for Averaging Pulsed Flow . . . . .	42
4.5 Pulsed Flow Results . . . . .	43
4.6 Physical Explanation of Results . . . . .	48
<b>Chapter 5 Conclusions</b> . . . . .	<b>50</b>
5.1 Future Work . . . . .	51
<b>REFERENCES</b> . . . . .	<b>52</b>
<b>Appendix A Part Drawings</b> . . . . .	<b>55</b>

<b>Appendix B Thermocouple Recovery Factor</b>	<b>62</b>
B.1 Introduction	62
B.2 Methods	64
B.2.1 Jet Production	64
B.2.2 Measurements	65
B.2.3 Procedure	67
B.3 Results	67
B.4 Conclusions	76
 <b>Appendix C Testing Procedures</b>	 <b>77</b>
C.1 System Checks	77
C.2 To do Every Run	78
C.3 Shut-down Procedures	78
 <b>Appendix D Sequential Perturbation Error Analysis</b>	 <b>79</b>

## LIST OF TABLES

2.1	Efficiency calculation comparison from Nango <i>et al.</i> . . . . .	13
3.1	Turbine inlet manifold experimental and CFD Mach numbers. . . . .	25
3.2	Calculated parameters and the measured input values. . . . .	31
4.1	Error and percent error for steady data. . . . .	38
4.2	Instrumentation and repeatability error. . . . .	39
4.3	JetCat mathematical model compared with the data for this thesis. . . . .	41
4.4	Pressure pulse amplitude (in kPa) for tested mass flows (in kg/sec). . . . .	44
B.1	Recovery factor error for grounded and exposed thermocouples. . . . .	71

## LIST OF FIGURES

1.1	First flight of PDE propelled aircraft. . . . .	1
1.2	The PDE cycle. . . . .	2
2.1	Brayton and Humphrey cycles. . . . .	7
2.2	Experimental setup of Rasheed <i>et al.</i> . . . . .	9
2.3	Experimental setup of Glaser <i>et al.</i> . . . . .	10
3.1	JetCat with and without combustor. . . . .	18
3.2	Test rig frame. . . . .	19
3.3	Test rig diagram. . . . .	20
3.4	Test rig. . . . .	21
3.5	ON/OFF valve, throttle valve, and pop-safety valve. . . . .	21
3.6	Sonic nozzle and surge tank. . . . .	21
3.7	Bypass valve, pulsing valve, and pulsing motor. . . . .	22
3.8	Turbine inlet pressure profile. . . . .	23
3.9	Plenum. . . . .	24
3.10	Turbine inlet manifold. . . . .	24
3.11	Turbine inlet manifold CFD streamlines. . . . .	26
3.12	Crack in the manifold. . . . .	26
3.13	Cross-sections of versions 1 and 2 of the inlet manifold. . . . .	27
3.14	Instrumentation diagram. . . . .	29
3.15	Lubrication tube. . . . .	32
4.1	Compressor map for the JetCat P-200. . . . .	36
4.2	Pressure ratio compressor map for the JetCat P-200. . . . .	37
4.3	Corrected mass flow vs. pressure ratio for steady flow. . . . .	40
4.4	Corrected mass flow vs. pressure ratio for steady flow and pulsed flow. . . . .	44
4.5	Turbine efficiency vs. pressure ratio for steady flow and pulsed flow. . . . .	46
4.6	Turbine map showing data collection line. . . . .	47
4.7	Specific work vs. pressure ratio for steady flow and pulsed flow. . . . .	48
A.1	Drawing of the compressor bore. . . . .	55
A.2	Drawing of the compressor backing. . . . .	56
A.3	Plate to attach the compressor housing to the test rig frame. . . . .	57
A.4	Plate to attach the turbine housing to the test rig frame. . . . .	58
A.5	Ball valve to coupling converter. . . . .	60
A.6	Ball valve packing nut and bearing. . . . .	61
A.7	Ball valve parts for test rig. . . . .	61
B.1	TSI 1127 Air Velocity Calibrator. . . . .	64
B.2	Diagram of a grounded and an exposed thermocouple. . . . .	65
B.3	Thermocouple position above plate. . . . .	66
B.4	Thermocouple position above nozzle. . . . .	67
B.5	Mean plenum and nozzle temperatures. . . . .	68



B.6	Mean plenum, nozzle, and static temperatures. . . . .	70
B.7	Calculated Mach number percent error. . . . .	71
B.8	Recovery factor for both types of thermocouples with error bars. . . . .	72
B.9	Plenum, nozzle, and corrected temperatures. . . . .	74
B.10	Amount of correction. . . . .	75

## NOMENCLATURE

### List of Abbreviations

AFRL	Air Force Research Laboratories
CAD	Computer Aided Design
CFD	Computational Fluid Dynamics
FEA	Finite Element Analysis
GTE	Gas Turbine Engine
PDE	Pulse Detonation Engine
PGC	Pressure Gain Combustion
WPAFB	Wright-Patterson Air Force Base

### List of Symbols

$\gamma$	Ratio of specific heats
$\eta$	Efficiency
$\Psi$	Weighting parameter
$\xi$	Time dummy variable
$\rho$	Density
$\tau$	Period
$c_p$	Constant pressure specific heat
$\dot{H}$	Enthalpy rate
$\dot{m}$	Mass flow rate
$M$	Mach number
$N$	Rotational speed
$p$	Pressure
$P$	Power
$r$	Recovery factor
$R$	Gas constant for air
$S$	Entropy
$T$	Temperature
$T_{junction}$	Temperature at thermocouple junction
$u$	Velocity
$w$	Specific work

### Subscripts and Superscripts

$[\ ]_0$	Total property
$[\ ]_c$	Corrected parameter
$[\ ]_e$	Exit quantity
$[\ ]_i$	Inlet quantity
$[\ ]_{stp}$	Standard temperature and pressure
$[\ ]^a$	Averaged
$[\ ]^{wa}$	Work averaged

## CHAPTER 1. INTRODUCTION

**I**N 2008, the Air Force Research Laboratory at Wright-Patterson Air Force Base became the first institution to successfully propel an aircraft using pulse detonation engines (PDEs) [1]. This historic feat proved to the world that PDEs have potential in aircraft propulsion. Pulse detonations offer several advantages when used in aircraft propulsion. However, there are also several hurdles inherent to the PDE cycle that inhibit the use of PDEs in aircraft propulsion. Although there are many potential applications of PDEs in aircraft propulsion, this thesis will focus on the integration of PDEs into gas turbine engines (GTEs), which involves replacing the conventional steady combustor with several PDE tubes.



Figure 1.1: First flight of PDE propelled aircraft. Image obtained from [http://www.afmc.af.mil/news/story\\_print.asp?id=123098900](http://www.afmc.af.mil/news/story_print.asp?id=123098900).

### 1.1 The Pulse Detonation Engine Cycle

Detonation is a pressure-gain, near constant-volume combustion process. The pulse detonation cycle consists of three main events: fill, fire, and purge as shown in Figure 1.2. During the fill stage a fuel-air mixture enters the pulse detonation tube. The fire stage is

further divided into four events. First, the fuel-air mixture is ignited. Second, the deflagration transitions to a detonation. This is known as deflagration to detonation transition and can be hastened by physical barriers. Third, the detonation propagates down the length of the tube. Fourth, rarefaction waves exhaust the combustion products from the tube. During the final stage of the pulse detonation cycle, or the purge stage, air enters the tube to push the rest of the exhaust products from the tube and to provide air for the next combustion event [2].

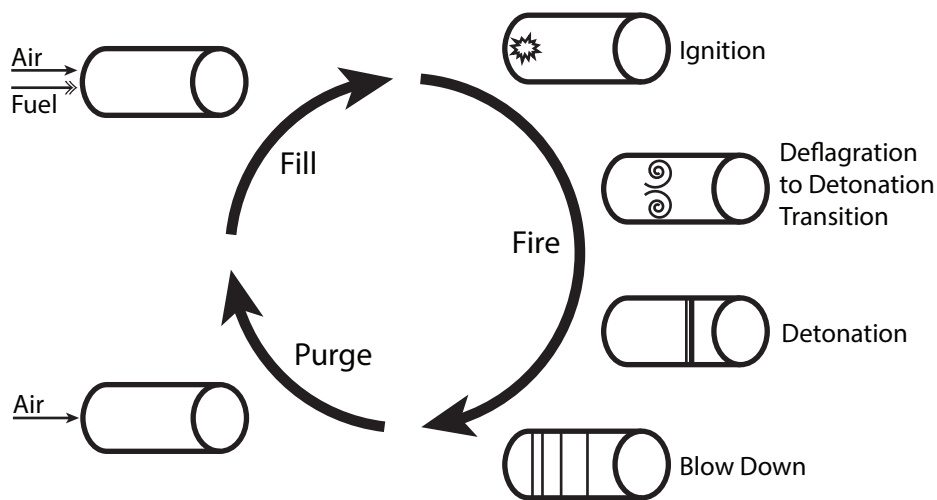


Figure 1.2: The PDE cycle.

## 1.2 Disadvantages of Pulse Detonation Engines

The main hurdles to using PDEs in aircraft propulsion are noise, the unsteadiness of the flow, and auxiliary power. Because the PDE cycle is basically a series of controlled explosions, using just PDEs for propulsion is very noisy. Dean *et al.* [3] showed that integrating a PDE with a conventional GTE decreased the decibel level of the noise produced by a PDE. Further investigation is necessary to determine whether GTE integration completely resolves the issue of noise.

Conventional turbines are designed for steady flow and replacing the conventional steady combustor with a PDE introduces highly unsteady flow at the turbine inlet. Unsteady

flow into a turbine can affect the efficiency, power generation, and fatigue life of the turbine. The turbine will operate off-design for most of the cycle because of the cyclical nature of the PDE cycle. Thus, one would expect the turbine efficiency and power generation to decrease when driven by pulsed detonations. The cyclical inlet pressure at the turbine inlet will also result in large fluctuations of the blade loading, which will affect the life of the turbine.

### 1.3 Advantages of Pulse Detonation Engines

There are three main advantages for aircraft propulsion that result from PDE/GTE integration. First, a PDE is able to operate across a wide range of Mach numbers including both the subsonic, sonic, and supersonic regimes since the combustion is a supersonic detonation instead of a subsonic deflagration. Second, the PDE cycle has decreased fuel consumption since it consumes fuel in short bursts instead of a constant stream. This fuel gain has been shown in PDE/GTE integration studies. Mawid [4] showed that the thrust specific fuel consumption decreased when using PDEs in place of a conventional afterburner. The decrease was 7.9% for a pulsing frequency of 50 Hz, 60.5% for 200 Hz, and 71.1% for 300 Hz. Petters and Felder [5] demonstrated that a turbofan with an integrated PDE had an 11% lower thrust specific fuel consumption than a conventional turbofan. Third, PDE/GTE integration decreases the number of necessary compressor stages to achieve a desired turbine inlet pressure [6, 7] since PDEs utilize pressure gain combustion. Decreasing the number of compressor stages allows more of the energy from the fuel to be used for thrust which results in increased efficiency. Decreasing the number of compressor stages also decreases the complexity of the engine.

As has been shown, integrating a PDE into a GTE is expected to increase engine performance. This may seem counterintuitive when recalling that the turbine efficiency and power is expected to decrease. However, recall the difference between cycle and component performance. While individual components, like the turbine, will show a decrease in performance, other components, such as the combustor and compressor, will show gains in performance. The sum of the gains and losses in performance are theorized to result in an increase in overall cycle performance.

## 1.4 Objective

Integrating PDEs into GTEs has the potential to increase GTE performance. Much work [2, 6–19] has been done to determine whether the advantages outweigh the disadvantages. This previous work will be discussed in greater detail in Chapter 2. As discussed above, using PDE exhaust to drive a turbine is problematic since this exhaust is inherently highly unsteady. Thus, a turbine driven by a PDE will need to accommodate a wide range of operating conditions [9].

The objective of this thesis is to determine the effect of cyclical pressure pulses on axial turbine performance. Previous research has used PDEs to drive both radial and axial turbines. The scope of this thesis is limited to axial turbines since this thesis considers the potential of PDEs in aircraft propulsion and aircraft engines primarily use axial turbines.

The experimental problem is simplified by using cold flow to isolate turbine performance under pulsed flow conditions. Using cold flow means that no combustion will occur and compressed air will be used to drive the turbine. The two main advantages of cold flow are instrumentation and full admission flow. Not using combustion allows the use of more sensitive instrumentation since the instrumentation does not need to withstand the high temperatures that occur with combustion events. More sensitive instrumentation decreases the experimental error. As will be reviewed in Chapter 2, some previous research has been unable to distinguish a difference between steady flow driven and PDE driven turbine performance within the error of the instrumentation.

Previous research that showed a difference in turbine performance under steady and pulsed flow has been limited to partial admission flow [17]. This limitation arises from driving the PDE tubes with an automotive head, which is an excellent method to control the flow of gases into the PDE tubes but can only fire one tube at a time. However, turbine performance is affected by partial admission flow. Cold flow allows this limitation to be avoided in favor of full-annular flow, limiting the effect on turbine performance to only the pulsing flow and not coupling it with partial admission.

In summary, the objective of this thesis is to measure the effect of pressure pulses on axial turbine performance by calculating turbine efficiency, pressure ratio, corrected mass flow, and specific work. This thesis adds significantly to the area of PDE/GTE integration

research in two ways. First, better experimental error is achieved by using more sensitive instrumentation. Second, the performance of an axial turbine driven by full-annular pressure pulses is compared to the performance of an axial turbine driven by steady flow.

## CHAPTER 2. LITERATURE REVIEW

This chapter reviews two main areas of work. The first section discusses previous work that has been done on integrating a PDE into a GTE. There are two main observations from this previous work. First, experiments done with axial turbines have involved other factors that could affect turbine performance, such as partial admission flow or bypass flow. Second, previous research concludes that turbine performance is negatively affected by pulsing flow. This result is expected after an analysis of the problem as discussed in Chapter 1. However, these results were obtained with a radial turbine and a partial admission axial turbine. This thesis isolates the effect of pressure pulses on axial turbine performance by using a full-admission pressure pulse.

The second section discusses different averaging methods. Comparing steady and pulsed flow requires that the pulsed flow be averaged by some method to yield single values for parameters such as efficiency and pressure ratio. An important observation is that averaging values results in a loss of information and it is important to choose an averaging technique that preserves the desired information.

Each section in this chapter is organized chronologically, except where there has been a continuation of a study, in which case the continuation follows directly after the initial study.

### 2.1 PDE/GTE Integration Studies

A numerical study performed by Hutchins and Metghalchi [20] in 2003 compared pressure gain combustion (PGC) and the conventional Brayton cycle (conventional GTE cycle). They used the Humphrey cycle to model the PGC, or pulse detonation cycle. Both of these cycles are shown in Figure 2.1. According to Hutchins and Metghalchi [20], although the Humphrey cycle is only similar to the PDE cycle, the detonation wave in the PDE



cycle allows it to be modeled as constant volume combustion. The results from this study should not be taken as representative of the real cycles, but since both the Humphrey and Brayton cycles were modeled in a numerically similar manner, the comparison is valid. This comparison showed that the Humphrey cycle was between 4 to 12% more efficient than the Brayton cycle, which demonstrates the potential gains of integrating a PDE with a GTE.

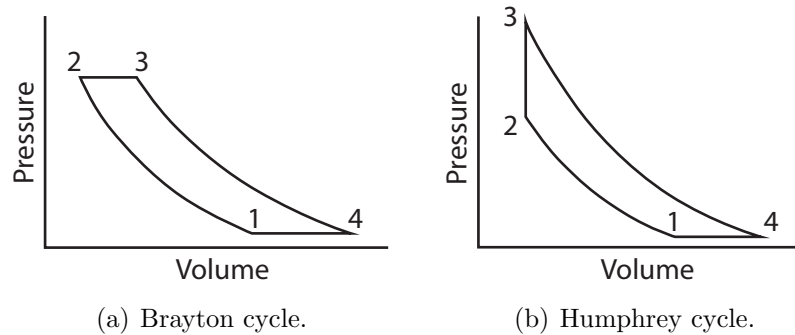


Figure 2.1: Brayton and Humphrey cycles.

Schauer *et al.* [8] studied the interaction of a PDE coupled with a turbocharger turbine with a converging nozzle at the turbine exit. They observed that the presence of the turbine dramatically increased the blowdown time by more than 5 times and caused back-pressuring of the PDE, which resulted in higher cycle initial pressures. The shock from the detonation reflected off the turbine, which resulted in only a weak pressure rise being observed downstream of the turbine. They compared the total work output of just a PDE tube and a PDE driven turbine and showed that the PDE driven turbine had about 4 times less work than just a thrust producing PDE tube.

In 2004, Rasheed *et al.* [9] obtained experimental and computational results for the interaction of PDE exhaust with a stationary 2D turbine cascade. They used a PDE tube combustor with a square cross-section that interfaced with the turbine cascade via a diverging section. The turbine cascade had 4 equally spaced blades. Optical grade acrylic sheets allowed shadowgraph images to be taken of the flow within the rotor passages. In their experiments, they focused on the interaction of the shock produced by the PDE with the turbine cascade. The shadowgraph visualization showed that there was a strong reflected

shock and a weak transmitted shock. The experimental geometry was then used to create a computational fluid dynamics (CFD) simulation, which used a single step chemistry mechanism to model the PDE combustion. In good agreement with the experimental results, the CFD results also showed a strong reflected shock and a weak transmitted shock. Overall, they found that mass flow through the PDE was affected by the presence of the turbine cascade and that PDE operation was not interrupted by the reflected shock.

In 2011, Rasheed *et al.* [12] performed a study with a 14 inch diameter single stage axial turbine driven by 8 pulse detonation tubes arranged in a can-annular configuration. Four different types of tests were performed. First, the turbine was driven by steady flow. Second, the turbine was driven by heated air. Third, a steady burner was placed upstream of the turbine. Fourth, pulse detonation tubes were fired into the turbine. Because of the size of the turbine, the flow from the PDE tubes alone was not enough to drive the turbine. To solve this problem, secondary air was added to the PDE air flow directly upstream of the turbine. Since this secondary air does not pass through the PDE tubes, it is called bypass air.

The results of this study [12] showed that no distinction in turbine performance could be determined within the uncertainty of the instrumentation. One explanation for this is that both bypass air and PDE exhaust enter a chamber 4.2 inches long before passing through the turbine, which would result in more steady flow than pulsed flow. The mixing region is shown in Figure 2.2. When the efficiency of the entire rig was estimated, the pulse detonation driven turbine showed a 4 percentage point increase in overall efficiency from steady state operation. This increase in overall efficiency of the rig was most likely due to the fuel benefits derived from using a PDE integrated with a turbine.

Glaser *et al.* [6] performed a study similar to the one performed by Rasheed *et al.* [12]. They compared results of a turbine driven by pulse detonation and constant-pressure deflagration. Both of these combustion methods were performed in the same tubes which exhausted into the turbine. The data showed that the efficiency of the pulse detonation driven turbine was comparable to the efficiency of the steady burner driven turbine. Similar to the experiment done by Rasheed *et al.* [10, 12], there was a chamber 7 tube diameters long between the pulse detonation tube exit and the turbine inlet where mixing with bypass




Figure 2.2: The experimental setup of Rasheed *et al.* [10,12]. Note the mixing plenum where the primary and secondary air mix.

air occurred. Only a maximum of 21% of the total turbine mass flow was combustion gases. The mixing chamber is shown in Figure 2.3.

While not using an axial turbine, Rouser *et al.* [2,11,13,16] obtained excellent results with a radial turbine. They showed that the turbine efficiency increased with pulsing frequency, although it was still less than the manufacturer's reported maximum efficiency. This increase in efficiency with pulsing frequency was attributed to shorter quiescent periods at the turbine inlet when using higher pulsing frequencies. In addition to efficiency, they showed that the specific work increased with increasing pulsing frequency. All of these comparisons were made with pulsing frequencies of 20 and 30 Hz.

St. George *et al.* [17,18] used an axial turbine and obtained comparable results to Rouser *et al.* [16]. Their setup included 6 PDE tubes arranged in a can-annular configuration with a sequential firing pattern. In contrast to Rasheed *et al.* [10,12] and Glaser *et al.* [6], they closely coupled the PDE tubes with the turbine so that there was no secondary flow. While their goal is to eventually perform fired PDE tests, their paper only considered cold

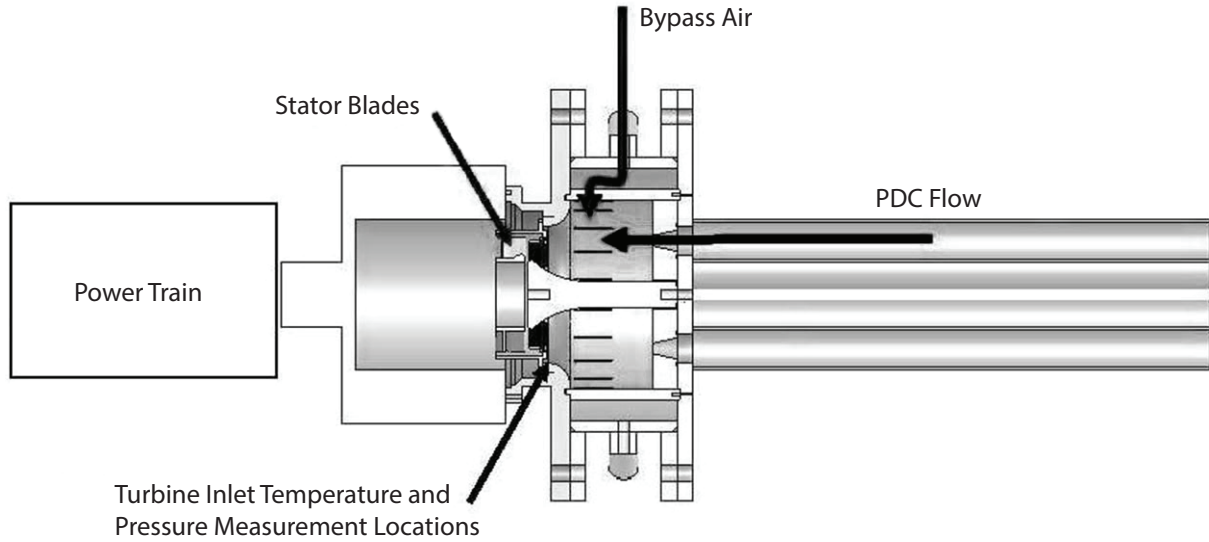


Figure 2.3: The experimental setup of Glaser *et al.* [6]. Note the region where both bypass air and PDC exhaust mix before entering the turbine.

pulsed flow. Their results showed a decrease in efficiency of about 15 percentage points from steady to pulsed flow and an increase in specific work with increasing pulsing frequency.

Ni *et al.* [19] performed a 2D CFD study of a turbine driven by pulsed flow. They used the geometry of an A3K7 Garrett power turbine with a simulated rotational speed of 25,200 rpm. Their pressure pulse had a duty cycle of 33%, an amplitude of 8.9 psia, and frequencies of 60 and 200 Hz. Their results showed that both specific work output and turbine efficiency decrease as the pulsing frequency was increased. Also, both specific work output and turbine efficiency were lower for a sequential firing pattern when compared with a synchronized firing pattern.

## 2.2 Averaging Methods

How to calculate efficiency is an important decision when considering a turbine driven by unsteady flow. Conventionally, turbine efficiency is defined as in Equation 2.1 for steady flow. While there is some fluctuation in the inlet and exit quantities, these values can be considered constant for steady flow. Because they are constant, there is no ambiguity which values to use in the equation for efficiency.

$$\eta = \frac{1 - \frac{T_{0e}}{T_{0i}}}{1 - \left(\frac{p_{0e}}{p_{0i}}\right)^{\frac{\gamma-1}{\gamma}}} \quad (2.1)$$

However, for unsteady flows, such as coupling a PDE to a turbine, there are large and rapid variations in inlet and exit quantities. Because of these variations, it is not intuitive which values should be used in the formulation of efficiency or even if the conventional equation for efficiency should be used. Several authors have investigated this issue and attempted to find the best formulation for unsteady efficiency, but there is still no accepted way to calculate the efficiency for unsteady flow. Their works are presented below.

In 2006, Cumpsty and Horlock [21] wrote an excellent paper on averaging non-uniform flow. The main point of their article was that the method of averaging is dependent on the use of the averaged value. Due to the nature of averaging, some information is lost when the flow quantities are averaged. Therefore, it is important to use a method that preserves the desired quantities.

Cumpsty and Horlock [21] presented four different methods of averaging non-uniform flows. Their methods assume constant specific heat for simplicity. The first method is an availability average and preserves the total enthalpy and availability flux of the flow. Since enthalpy and availability both are directly related to temperature for constant  $c_p$ , the average temperature reduces to a simple mass average.

$$\dot{m}T_0^a = \int T_0 d\dot{m} \quad (2.2)$$

The average total pressure is then found using

$$\ln p_0^a = \frac{1}{\dot{m}} \int \ln p_0 d\dot{m} - \frac{\gamma}{(\gamma-1)\dot{m}} \int \ln \frac{T_0}{T_0^a} d\dot{m} \quad (2.3)$$

The disadvantage of this method is that it will over-predict the total pressure if there is a uniform pressure field, but a non-uniform temperature field. With a uniform pressure field, one might think to just use the total pressure of the field as the average value since the field

is uniform. However, this is not the case. If there is a variation in the temperature field, there is more potential to do work because of this temperature difference. Averaging the temperature removes this work potential. According to this method, in order to compensate for this loss in work potential and preserve the total the enthalpy and availability of the flow, the average total pressure must increase.

The second method is a work average and preserves the work input into or work output from a turbomachine. This method is ideal when the work input, work output, pressure ratio, or efficiency are of interest. Again, since enthalpy scales directly with temperature for constant  $c_p$ , the average total temperature can be determined using a simple mass average as shown in Equation 2.2. The average total pressure is then determined using

$$p_0^{wa} = \left[ \frac{\int T_0 d\dot{m}}{\int \frac{T_0}{p_0^{(\gamma-1)/\gamma}} d\dot{m}} \right]^{\gamma/(\gamma-1)} \quad (2.4)$$

The third method is a thrust average and preserves the same thrust as the flow being averaged. The fourth method is a nozzle average, which preserves the mass flow capacity. The equations for the last two methods will not be presented here as these methods are for nozzles and choked turbine nozzle rows, neither of which are applicable to this thesis.

Nango *et al.* [22] performed a numerical simulation of a PDE driven turbine in 2009. The 2D simulation used midspan geometry from a Japan Aerospace Exploration Agency hypersonic turbojet engine. The simulation was run at 6 different rotor speeds ranging from 10% to 150% of design speed with a pulsing frequency of 1000 Hz. They compared two different methods of calculating turbine performance. The first method used an energy balance and integrated the enthalpy flow over the cycle to determine the turbine actual and ideal work. The ideal work was obtained by using an ideal exit pressure. The second method integrated the pressure over the rotor blade to determine turbine work. A comparison between these two methods is shown in Table 2.1. They did not make any comparison to steady flow.

Suresh *et al.* [23] presented and compared two different formulations to calculate turbine efficiency under pulsed flow. The first method was referred to as the time-resolved

Table 2.1: Efficiency calculation comparison from Nango *et al.* using the energy balance method and the mechanical approach. For percent difference the mechanical efficiency values are compared to the energy balance efficiency values.

% Rotor Speed	Energy Balance Efficiency	Mechanical Efficiency	% Difference
10	9.3	5.1	-45.16%
50	29.0	21.6	-25.52%
80	38.3	33.5	-12.53%
100	42.7	40.3	-5.62%
120	45.6	46.3	1.54%
150	48.3	53.1	9.94%

method and integrated the turbine performance over the cycle. This method assumed that the expansion through the turbine occurred instantaneously. This method is shown in Equation 2.5. Note that turbine power,  $P$ , can be obtained by multiplying the torque by the angular speed.

$$\eta^a = \frac{\int_0^\tau P dt}{c_p \int_0^\tau \dot{m}_i T_{0i} \left( 1 - \left( \frac{p_{0e}}{p_{0i}} \right)^{(\gamma-1)/\gamma} \right) dt} \quad (2.5)$$

The second method is a definition based on work averaging. This method generated averaged values that preserve the work output of the turbine, the work inflow, and the work outflow. Thus, using the averaged values to calculate the turbine work output would yield the same value as using an integral approach. The same is true with calculating the work potential of the entering and exiting fluid. This method is the same as the work averaging method presented by Cumpsty and Horlock [21], but more details specific to pulsed flow through a turbine are presented by Suresh *et al.* [23]. This method is shown in Equations 2.6-2.9.

$$T_0^a = \frac{\int_0^\tau \rho u T_0 d\xi}{\int_0^\tau \rho u d\xi} \quad (2.6)$$

$$(p_{0i}^{wa})^{(\gamma-1)/\gamma} = \frac{\int_0^\tau \rho_i u_i T_{0i}(\xi) d\xi}{\int_0^\tau \rho_i u_i \left( \frac{T_{0i}(\xi)}{p_{0i}(\xi)^{(\gamma-1)/\gamma}} \right) d\xi} \quad (2.7)$$

$$(p_{0e}^{wa})^{(\gamma-1)/\gamma} = \frac{1}{\tau} \int_0^\tau p_{0e}^{(\gamma-1)/\gamma}(\xi) d\xi \quad (2.8)$$

$$\eta^{wa} = \frac{T_{0i}^a - T_{0e}^a}{T_{0i}^a (1 - (p_{0e}^{wa}/p_{0i}^{wa})^{(\gamma-1)/\gamma})} \quad (2.9)$$

Rouser *et al.* [16] showed that turbine efficiency under pulsed conditions can vary depending on the formulation used to calculate efficiency. Because of the constantly changing quantities and mass storage associated with unsteady flows, they maintain that an integrated approach needs to be used to calculate the turbine efficiency driven by an unsteady flow. One method is to use a time-integration to obtain an instantaneous turbine efficiency. However, the turbine inlet and exit values are not connected in time because of the rapidly changing values. This makes a time-integrated approach impractical for experimental studies because it is difficult to establish a relationship between the inlet and exit properties of each mass unit traveling through the turbine. A second method is to determine a cycle average efficiency by using the net total enthalpy at the inlet and exit of the turbine. This method is shown in Equation 2.10.

$$\eta^a = \frac{\int_{cycle} \dot{H}_{0i} dt - \int_{cycle} \dot{H}_{0e} dt}{\int_{cycle} \dot{H}_{0i} \left( 1 - \left( \frac{p_{0e}}{p_{0i}} \right)^{\frac{\gamma-1}{\gamma}} \right) dt} \quad (2.10)$$

A weighting parameter was then applied to the pressure ratio term to account for variations in the mass flow rate. Given a fixed pressure ratio, a low mass flow rate will have



less potential to do work than a higher mass flow rate. The weighting parameter provides a way to connect the pressure ratio with a flow quantity. Equation 2.11 shows how the weighting parameter is applied and Equation 2.12 combines Equations 2.10 and 2.11.

$$\left[ \left( \frac{p_{0e}}{p_{0i}} \right)^{\frac{\gamma-1}{\gamma}} \right]^a = \frac{\int_{cycle} \Psi \left( \frac{p_{0e}}{p_{0i}} \right)^{\frac{\gamma-1}{\gamma}} dt}{\int_{cycle} \Psi dt} \quad (2.11)$$

$$\eta^a = \frac{\int_{cycle} \dot{H}_{0i} dt - \int_{cycle} \dot{H}_{0e} dt}{\left( 1 - \left[ \left( \frac{p_{0e}}{p_{0i}} \right)^{\frac{\gamma-1}{\gamma}} \right]^a \right) \int_{cycle} \dot{H}_{0i} dt} \quad (2.12)$$

Rouser *et al.* [16] used two different weighting parameters, mass flow and total enthalpy, to calculate the turbine efficiency. Using these two parameters, the difference in efficiency was at most 5 percentage points. They also calculated the efficiency with no weighting parameters, but this method yielded efficiency values greater than the manufacturer's reported maximum turbine efficiency. Efficiency values greater than the manufacturer's reported maximum efficiency are not reasonable because the turbine is operating off-design for most of the cycle. Thus, it cannot be expected that the turbine would be more efficient. The weighted turbine efficiency values were approximately 20 percentage points lower than this maximum value.

Ni *et al.* [19] performed a 2D CFD study of a turbine driven by pulsed flow. Using the results from the simulations, they compared three different methods to calculate the average cycle efficiency: mass-weighted moving average of temperature and pressure (TP), mass-weighted moving average of temperature and entropy (TS), and specific work output and entropy increase (WS). In the TP method, mass-weighted moving average values for temperature and pressure were used in the conventional equation for turbine efficiency shown in Equation 2.1. The TS method used mass-weighted averages for total temperature and entropy in Equation 2.13 to determine the efficiency.

$$\eta^a = \frac{T_{0i}^a - T_e^a}{T_{0i}^a - T_{0e}^a e^{(S_e^a - S_i^a)}} \quad (2.13)$$

The final method, WS, calculated the efficiency based on the specific work output and the energy lost by entropy increase. The average specific work was determined with a time integral. The turbine efficiency was then calculated as shown in Equation 2.14.

$$\eta^a = \frac{w}{w + c_p T_{0e}^a (1 - e^{(S_e^a - S_i^a)})} \quad (2.14)$$

They found that the TP method yielded efficiency values about 5 percentage points lower than the other methods for rotor efficiency, but very comparable efficiency values for stage efficiency.

All of these averaging techniques were considered when deciding how to analyze the pulsed flow data. According to the work of Cumpsty and Horlock [21], it is important to select an averaging method to preserve information about the quantities of interest. For this thesis, the quantities of interest were the turbine mass flow, turbine work, turbine pressure ratio, and turbine efficiency. Thus, the most appropriate averaging method was a work average since it preserves these quantities. The work averaging method presented by Suresh *et al.* [23] was the most detailed and applicable to the work of this thesis and so it was chosen for the averaging method.

## CHAPTER 3. RIG DESIGN AND EXPERIMENTAL METHODS

The research facility uses a JetCat P-200 gas turbine engine as the testbed. This turbine was chosen for its simplicity and relatively low cost. Conventionally, the JetCat P-200 is a hobbyist engine commonly used on model jet aircraft and has a single stage radial compressor and a single stage axial turbine. The engine runs at speeds between 32000 and 112000 rpm, has a maximum thrust of 52 lbs, has a mass flow rate of 1 lbm/sec, and weighs 5 lbs [24]. This engine has also been used by the Air Force Research Laboratory (AFRL) at Wright-Patterson Air Force Base (WPAFB) in Dayton, Ohio as a test bed for many experiments.

### 3.1 JetCat Modification

In lieu of a combustor, the engine was modified to allow compressed air to be ducted into the turbine. First, the outer casing of the JetCat was removed to expose the combustor and is shown in Figure 3.1(a). Second, the combustor was removed from the JetCat by cutting it off with a cut-off tool. The JetCat with the combustor removed is shown in Figure 3.1(b). Without the outer casing on the engine, the turbine housing was not secured in place and it was possible to shift the turbine housing to come in contact with the turbine wheel. Unless the turbine housing was aligned correctly, the turbine blades would rub against the housing and in some cases there was enough friction to prevent the turbine from rotating at all. Removing the combustor exacerbated this issue. Because it was important for the turbine to not contact the turbine housing, a mounting system that would provide alignment capabilities and was easy to manufacture was needed. With these two design considerations, it was decided to construct the turbine mounting structure from T-slotted aluminum framing, which would provide the needed stability, but also be adjustable to achieve the correct

alignment. This frame was also made large enough so that instrumentation and inlet/exit ducting could also be mounted on the frame. The aluminum frame is shown in Figure 3.2.

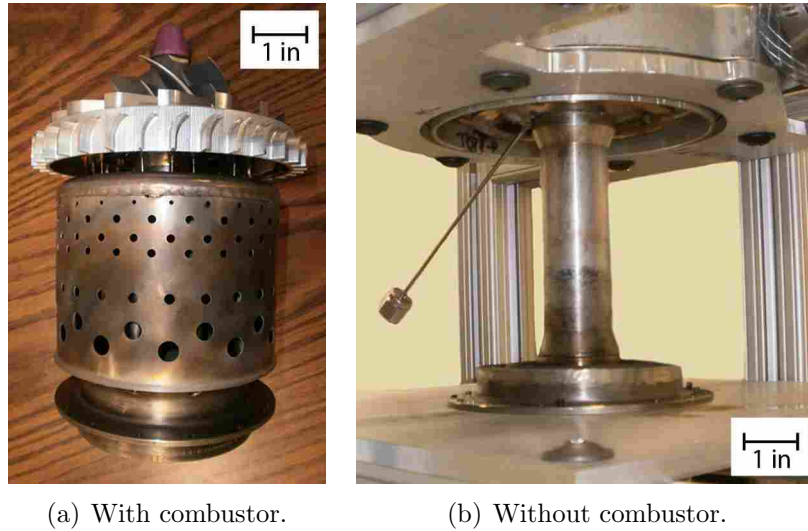


Figure 3.1: JetCat with and without combustor.

### 3.2 Rig Air Flow

There are two separate air pathways in the rig shown in Figures 3.3 and 3.4. The first air pathway comes from the compressed air tank, through a sonic nozzle and into the turbine. The second pathway is through the compressor. The compressor and turbine are only coupled via a shaft, which allows the compressor to act as a dynamometer and brake the turbine.

The turbine air pathway begins with a compressed air tank that holds approximately 1100 cubic feet of air at 150 psi. At the exit of this tank there is a 2 inch full port ball valve that turns the flow of air on and off. Downstream of this valve is the throttle valve, which is used to set the mass flow out of the compressed air tank. This valve is a 2 inch gate valve with a rising stem so it can be set at a specified number of turns open. Just downstream of the throttle valve is a pop-safety valve set to 150 psi with a rated flow rate of 1244 scfm. The three valves just discussed are shown in Figure 3.5. About 50 feet of braided nylon hose with a 2 inch diameter and rated at 150 psi is used to transport the air from the tank exit to

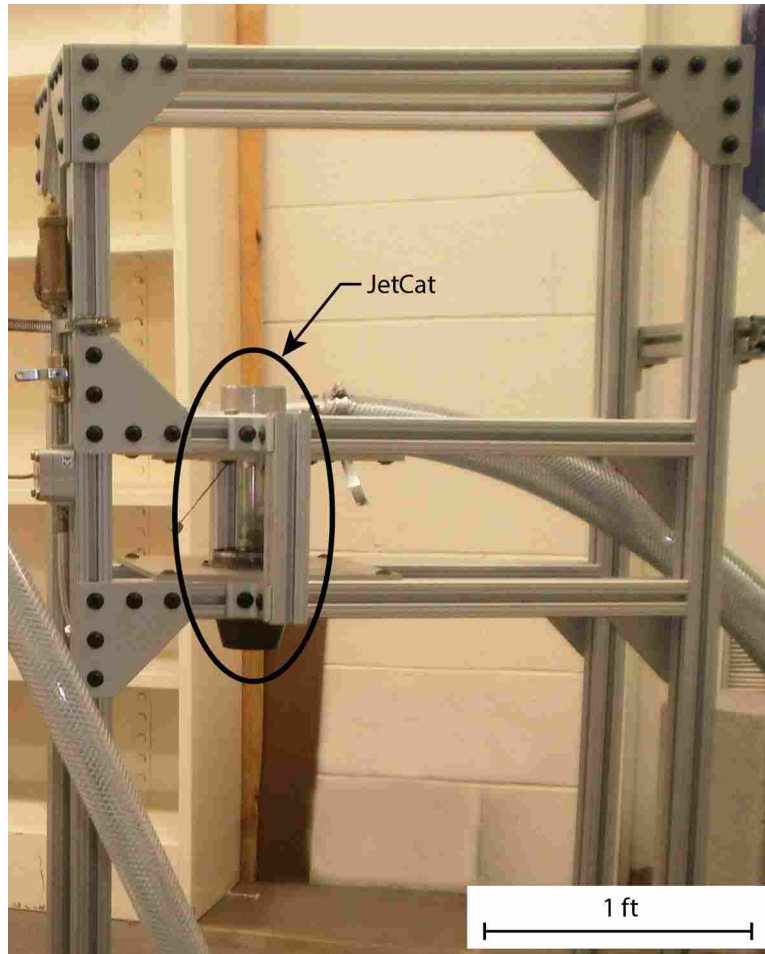


Figure 3.2: JetCat in the test rig frame.

the rig. This hose is connected to the inlet of a sonic nozzle run, which is used to measure the mass flow of air into the turbine. Downstream of the sonic nozzle there is a 20 gallon surge tank to damp out the pressure pulses created during pulsed testing and prevent these pressure pulses from unchoking the sonic nozzle. The sonic nozzle and surge tank are shown in Figure 3.6.

### 3.2.1 Bypass and Pulsing Valves

During testing it became clear that a surge tank alone was not enough to prevent the sonic nozzle from unchoking. In addition to the surge tank, a bypass valve was installed around the pulsing valve to prevent a complete stopping of the flow. The bypass valve was

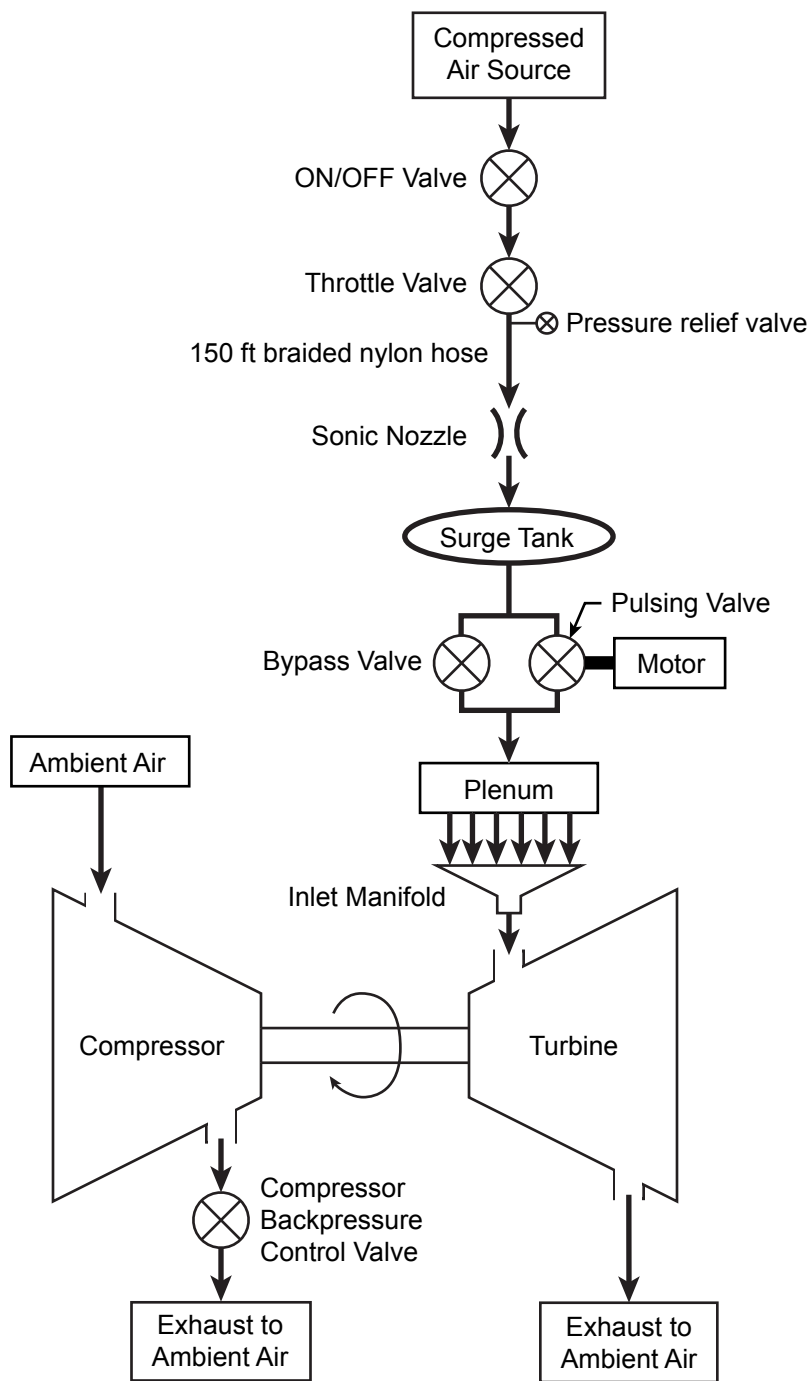


Figure 3.3: Test rig diagram.

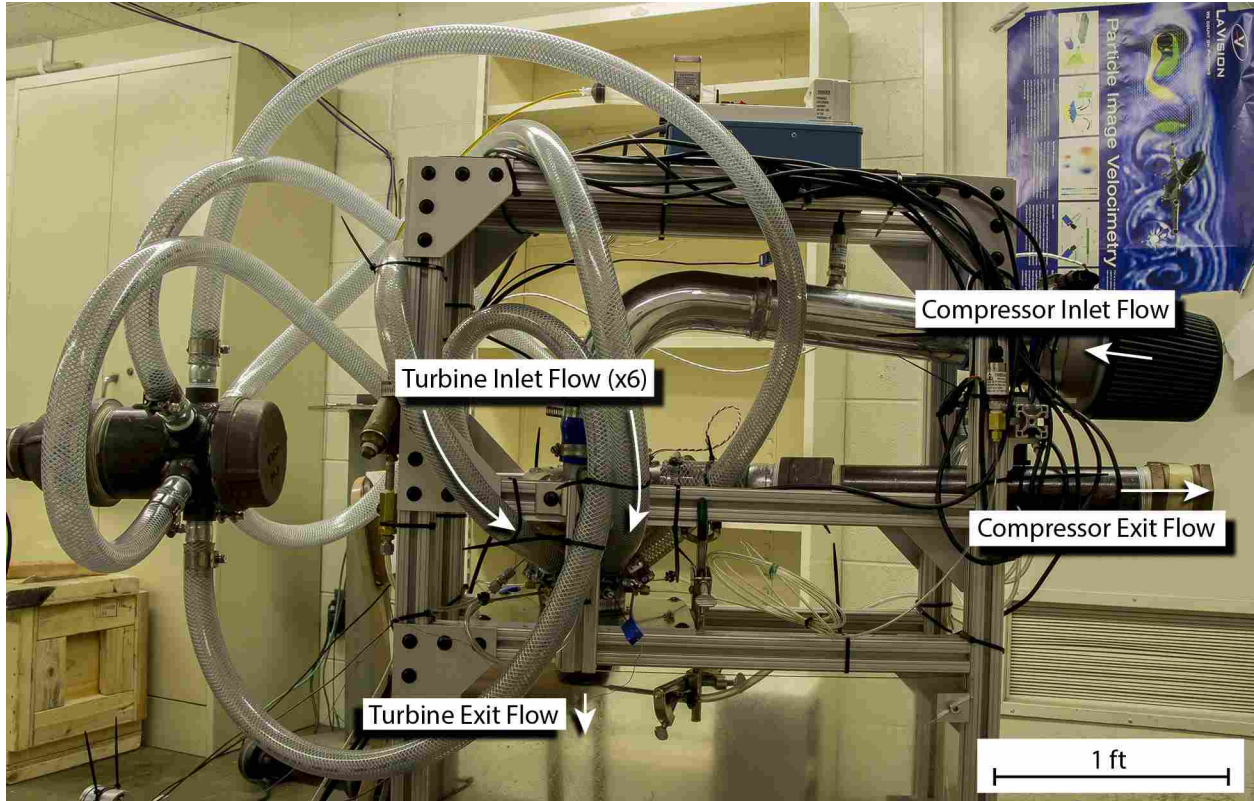


Figure 3.4: Test rig with turbine and compressor air paths labeled.



Figure 3.5: ON/OFF valve, throttle valve, and pop-safety valve. The pipe size in this figure is 2 inches.

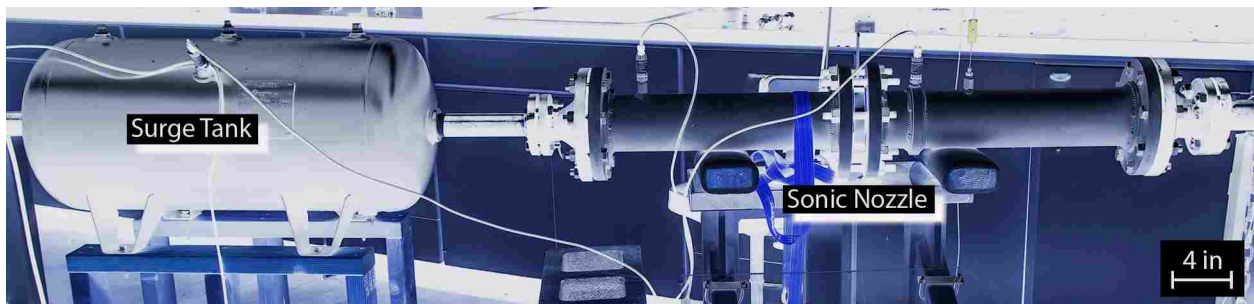


Figure 3.6: Sonic nozzle and surge tank. The sonic nozzle run is 4 inch pipe.

adjusted to allow the minimum amount of air past to maintain the sonic nozzle in a choked state. The bypass valve is shown in Figure 3.7.

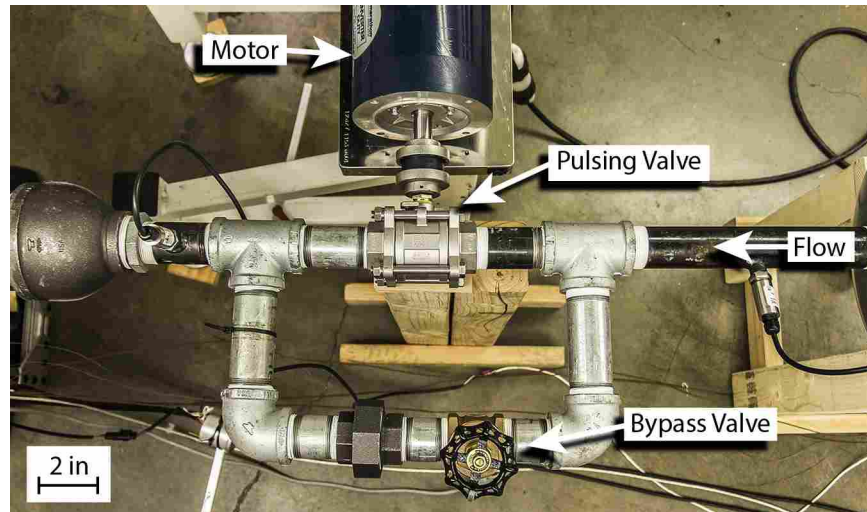


Figure 3.7: Bypass valve, pulsing valve, and motor. The pipe size in this figure is 1.5 inches.

Pressure pulses are generated by rotating a ball valve with an electric motor, also shown in Figure 3.7. The ball valve is a 1.5 inch diameter, full port, stainless steel ball valve with replaceable packing. Since the valve will be spinning at speeds of 300 rpm up to 1200 rpm, it was desirable to have an easy way to replace parts of the ball valve that would become worn out. The motor is a Marathon Electric E2007 inverter duty motor with a maximum rpm of 1745, a minimum rpm of 175, and a horsepower rating of 2 hp. The motor was controlled with an Automation Direct GS2-22P0 motor controller.

Other actuated valves were considered, but found to be inadequate to provide pressure pulses at a frequency of 10 to 40 Hz, which was the desired range of pulsing frequencies. Rotating a ball valve with an electric motor was used since ball valves can rotate freely when the handle is detached. Remember that in this thesis the experimental problem is simplified to isolate the issue of pulsed flow, so a simple sinusoidal pressure pulse was desired at the turbine inlet. Figure 3.8 shows the turbine inlet pressure profile for a mass flow of 0.64 kg/sec and a pulsing frequency of 10 Hz and demonstrates that the desired turbine inlet pressure profile was obtained.



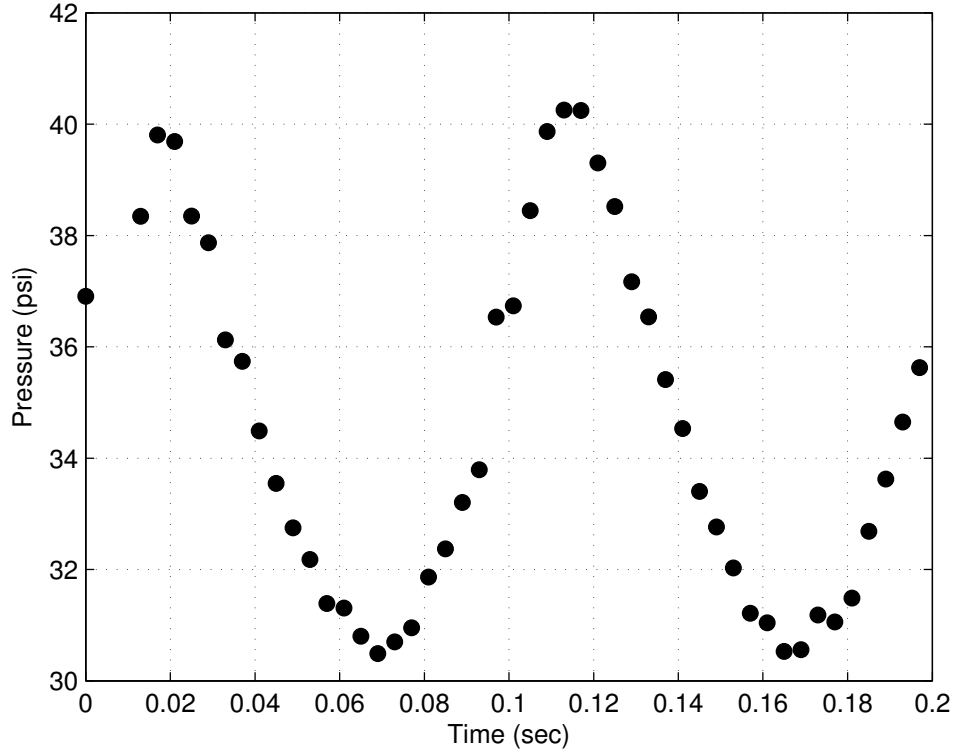


Figure 3.8: Turbine inlet pressure profile for a mass flow of 0.64 kg/sec and a pulsing frequency of 10 Hz.

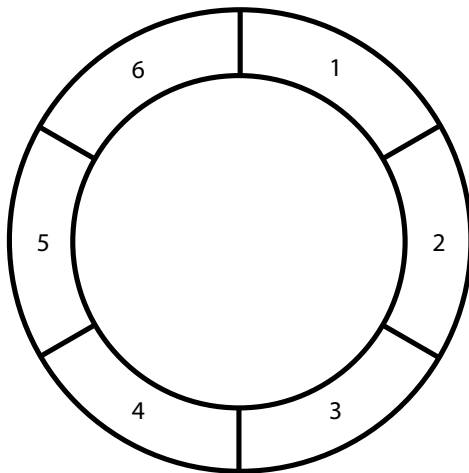
### 3.2.2 Plenum and Inlet Manifold

One of the difficulties of using an axial turbine without a conventional combustor is transitioning the flow into the turbine. This difficulty is encountered when using tube PDEs or compressed air to drive the turbine. In our specific case, the air needed to transition from a single pipe to an annular shape of six sectors. Downstream of the pulsing and bypass valves, air enters a plenum, where it is split into six different air streams. The plenum was designed with six exits placed in a radial pattern perpendicular to the incoming flow of air so that equal flow would be provided to each of the six exits. The plenum is shown in Figure 3.9.

These six air streams are conducted via braided hose to the inlet manifold, which recombines the six different air streams into a six-sectored annulus just upstream of the turbine. The inlet manifold and annular flow configuration into the turbine are shown in Figure 3.10. After the turbine, the air is exhausted into ambient air.



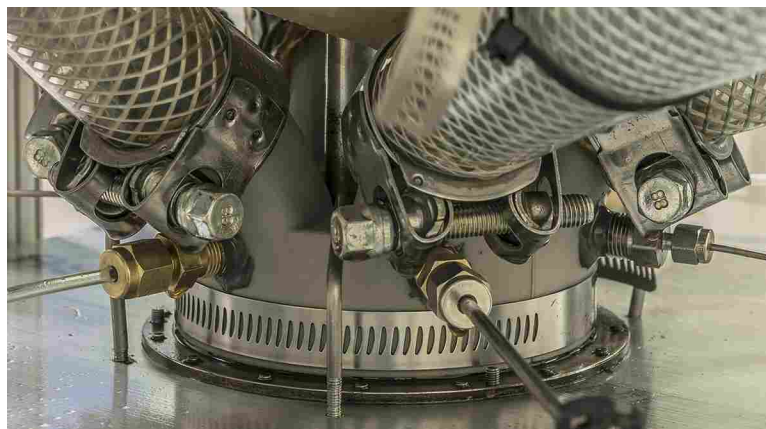
Figure 3.9: Flow dividing plenum. The plenum was made from 4 inch pipe.



(a) Turbine inlet configuration.



(b) Turbine inlet manifold.



(c) Installed inlet manifold.

Figure 3.10: Turbine inlet configuration, inlet manifold CAD model, and installed turbine inlet manifold. The inlet manifold is connected to the plenum with 1 inch diameter hose.

The inlet manifold was evaluated to determine if there would be any flow separation that would affect pressure measurements taken within the manifold. This evaluation was done with a CFD simulation in STAR-CCM+ of the inlet manifold. The results of this simulation are shown in Figure 3.11 where the streamlines show that there is no flow separation. These results are expected because the turbine inlet manifold is basically a nozzle. This geometry results in a favorable pressure gradient, which prevents flow separation. It should be noted that the Mach numbers calculated by the simulation are comparable to the experimentally determined Mach numbers as shown in Table 3.1.

Table 3.1: Comparison of turbine inlet manifold Mach numbers from experimental and CFD results.

<b>Experimental</b>		<b>CFD</b>	
Mass Flow	Mach Number	Mass Flow	Mach Number
0.37	0.29	0.36	0.26
0.47	0.30	0.49	0.29
0.63	0.31	0.65	0.33

Initially, the turbine inlet manifold was made using a fused deposition rapid prototyping machine. After using this manifold for 16.5 minutes of run-time, cracking and deformation occurred. The manifold crack is shown in Figure 3.12. Possible reasons for this cracking included the fused deposition layering method used in making the inlet manifold and the weight of the hoses. The fused deposition layering method of manufacture created discrete layers which could peel apart if enough force was applied. When the hoses were attached to the inlet manifold, they were also attached to the aluminum frame with zip ties. However, some of the weight from the hoses still rested on the inlet manifold. FEA analysis was used to verify the possible explanations with the cracking locations.

Two modifications were made to the inlet manifold to prevent future cracking and deformation. First, the design was modified to add more material to the spots that cracked and deformed. This is shown in Figure 3.13 where cross-sections of manifold designs 1 and 2 are shown. Second, the new design was then manufactured as a glass filled nylon rapid

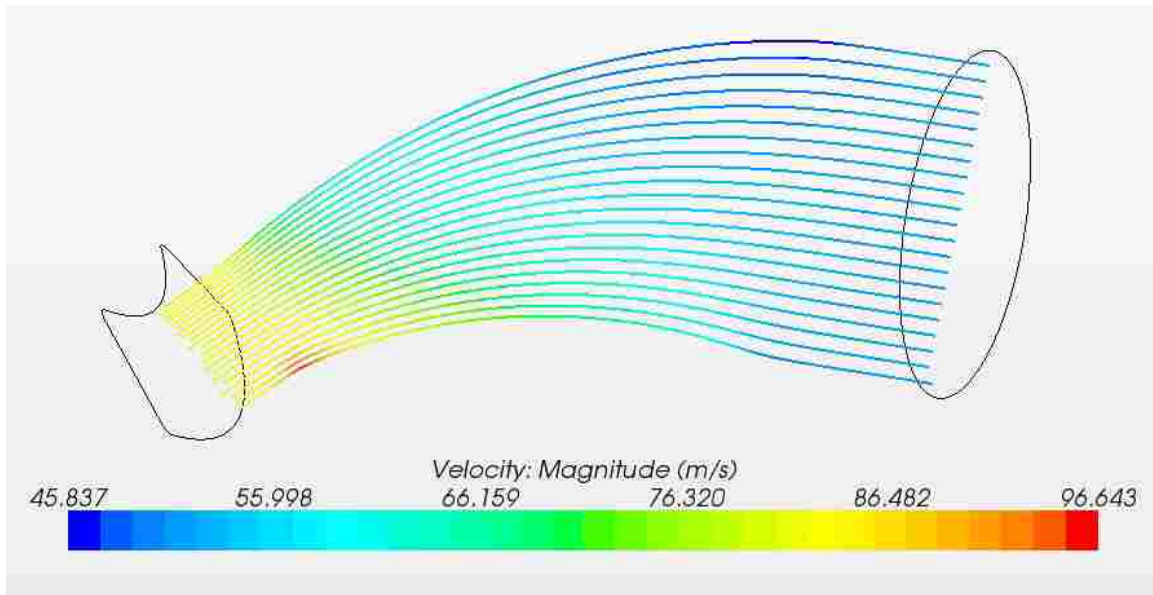


Figure 3.11: CFD simulation of one section of the turbine inlet manifold showing streamlines of velocity magnitude. Flow is from right to left and the inlet is about 1 inch in diameter.



Figure 3.12: Crack in the manifold.

prototype instead of a fused deposition rapid prototype. The modified inlet manifold has held up well in testing for 70.5 minutes of runtime and does not show any of the deformation and cracking problems exhibited by the previous inlet manifold.

### 3.2.3 Compressor Air Flow

The compressor has a separate air flow pathway. Ambient air is drawn into the compressor through a mass air flow sensor. A modified Garrett turbocharger housing was used for the JetCat radial compressor to duct the compressor air flow through the compressor

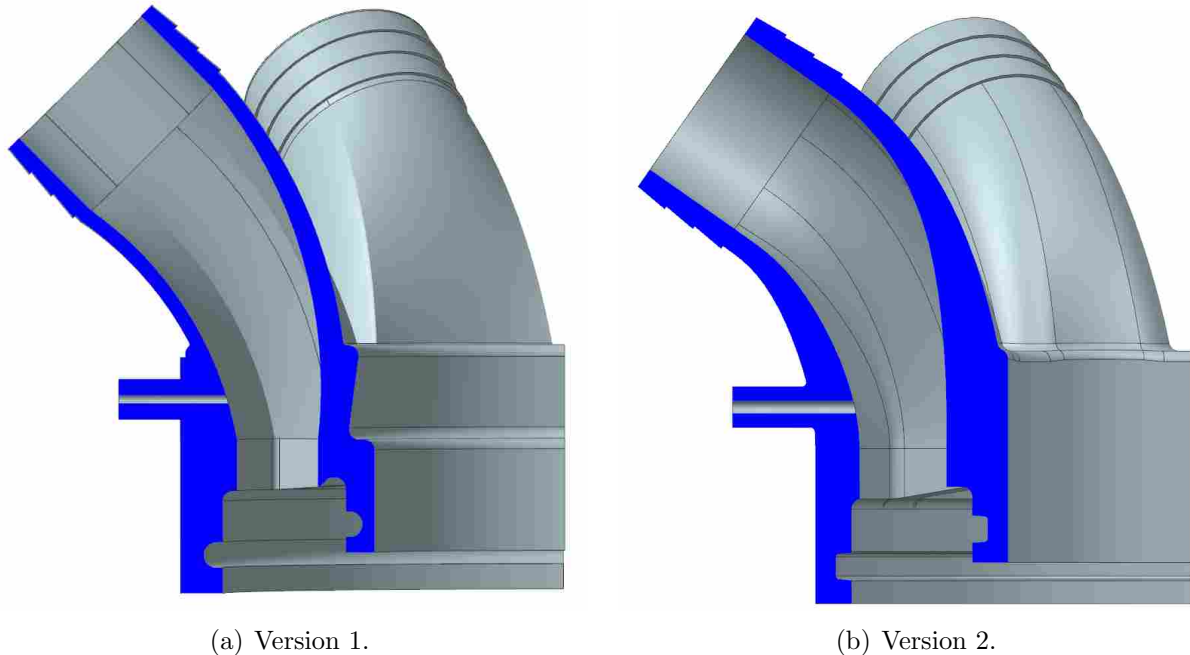


Figure 3.13: Versions 1 and 2 of the turbine inlet manifold. Version 2 is the re-design of version 1 after the discovery of cracking and deformation. Flow enters the inlet manifold from the top left hand corner of both figures and exits at the bottom of the figure. The barbed interface connects to 1 inch diameter hose.

and allow measurement of inlet and exit quantities. This housing was the same used by Tellefsen [14] with part number 756021-1. The housing inlet was machined to fit the JetCat compressor since it is not manufactured specifically for the JetCat. The drawing for the machining of the inlet is shown in Appendix A. The compressor exit is equipped with a 2 inch gate valve to control the compressor back pressure.

### 3.2.4 Rig Air Flow Control Summary

To clarify, the test rig air flow is controlled by three different valves. There is a 2 inch ball valve at the exit of the compressed air tank that turns the air flow through the turbine on or off. This valve is either completely open or completely closed. About 4 feet downstream of this valve is the throttling valve, which sets the mass flow through the turbine. The throttling valve is a gate valve that is set a certain number of turns open to allow for different mass flows through the turbine. This valve changes the upstream pressure on the sonic nozzle. Since the mass flow through the sonic nozzle is choked, the mass flow

is based on the upstream pressure. Finally, there is a gate valve at the compressor exit to control the back-pressure on the compressor. This controls the compressor operating point and the mass air flow through the compressor by controlling the compressor pressure ratio.

### 3.3 Instrumentation

Data acquisition was done using LabVIEW software and a National Instruments cDAQ-9174 with modules 9205, 9213, 9265, and 9401. The cDAQ was chosen because it would allow control of a motor, could collect data at 250 Hz, and had module capability. Because the pulsing valve would be driven by a motor, it was desired to integrate motor control capabilities into the LabVIEW program. Pulsing frequencies of up to 40 Hz would be used, which yielded a data acquisition Nyquist frequency of 80 Hz. However, a higher data acquisition frequency was chosen to achieve a higher pulse resolution. Different signal inputs such as pressure transducer voltage, thermocouple voltage, and digital signals needed to be collected. Additionally, voltage and current output signals were needed. Module capability allowed all of these input and output needs to be met in one device. A cRIO chassis was also considered and tested, but with 22 channels of input the cRIO was not able to maintain a 250 Hz data acquisition rate.

An instrumentation diagram that summarizes the instrumentation types and locations is shown in Figure 3.14. The pressures were measured with PX-309 pressure transducers purchased from Omega. These pressure transducers were chosen because they have a 0 to 5 V output. When developing the LabVIEW program it was discovered that pressure transducers with an output of 0 to 20 mA had an unacceptable level of noise with the cRIO platform. The decision to use the PX-309 pressure transducers was made before the decision to switch to the cDAQ platform. The PX-309 pressure transducers worked well with both the cRIO and cDAQ platforms.

When first testing running the pulsing valve with flow, it was found that there were high levels of noise in the pressure transducer signals when the motor was running. The noise levels were on the order of volts and were overwhelming the actual signal, which had an output of 0 to 5 V. Each pressure transducer has 3 wires, two for power and one for ground. When building the rig, all the power lines had been connected to the rig power with

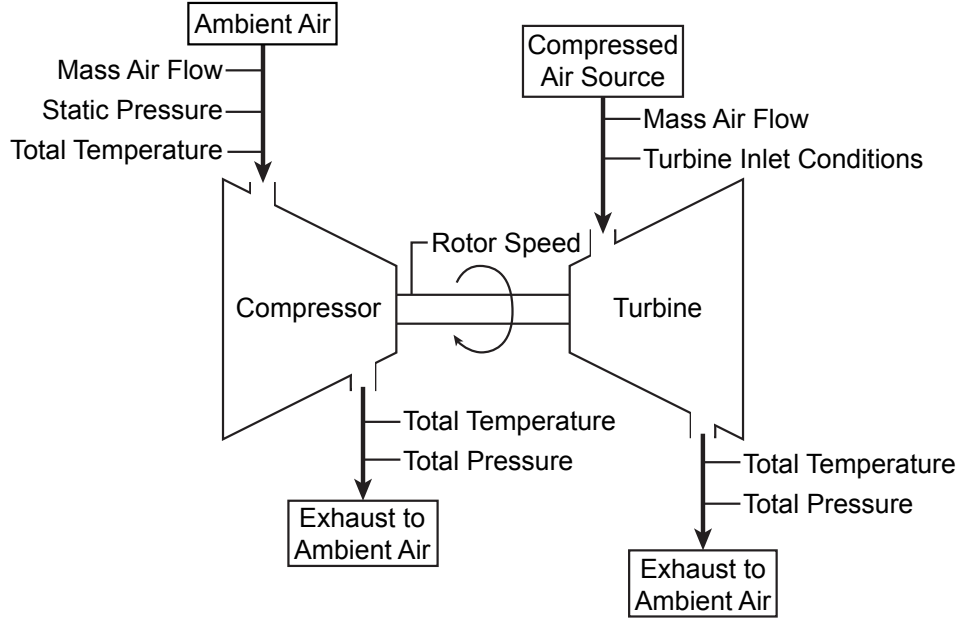


Figure 3.14: Instrumentation on experimental test rig.

one cable and all the signal lines had been connected to the data acquisition system with another cable. This was done to maintain organization in the wiring. Both the power and signal cables had braided shielding, but it was discovered that running all three pressure transducer connections through the same cable solved the noise issue. It was thought that even though both cables had shielding, the shielding was not equal between both cables, which would result in an unequal removal of noise between the two cables. All three wires from each pressure transducer needed to run through the same cable. All of the pressure transducers were still split between two cables, but the wires from each pressure transducer were going through a single cable. After this was done, the noise was reduced to levels within the error of the pressure transducers.

Static pressure measurements were performed with a conventional wall tap and total pressure measurements were taken utilizing a Kiel probe. Two sizes of Kiel probes were purchased from United Sensor, Inc. A 0.125 inch probe (KAC-6) was used in the inlet manifold and a 0.25 inch probe (KBC-6-F-5) was used at the turbine and compressor exit. The temperatures were measured with  $1/16$  inch, sheathed, type T thermocouples, also purchased from Omega. The rotor speed was measured on the compressor side with a Garrett tur-

bocharger speed sensor with part number 781328-0001. The speed sensor uses eddy currents to measure the speed since the compressor is made from aluminum. Because the sensor uses eddy currents, the compressor must be rotating at a speed greater than 5000 rpm for the sensor to register. A Pro-M 92 mass air flow meter with a maximum flow rate of 60 lb/min and a 30 point calibration was used to measure the compressor inlet mass flow rate and a 1 inch diameter sonic nozzle purchased from Flow Systems, Inc. was used to measure the turbine inlet mass flow rate. There are six turbine inlet conditions that were measured, one in each of the manifold inlet passages. The total temperature was measured in two of the inlet passages. The other four passages are used to measure pressure. Two passages contain total pressure measurements and the other two passages contain static pressure measurements.

The measured values used in the calculations of the turbine performance parameters are shown in Table 3.2. Other measured values were used to ensure proper rig operation. Calculation of the sonic nozzle mass flow and total temperatures are not listed in the table because they are not turbine performance parameters, but involve subtleties that are now discussed. The mass flow through the sonic nozzle was calculated using an upstream static pressure, an upstream temperature, and calibration data provided by a calibration company, Colorado Engineering Experiment Station, Inc. Thermocouple measurements were corrected to total temperature using an experimentally determined recovery factor of 0.815. Spatial and monetary constraints did not permit the use of total temperature probes and regular sheathed thermocouples result in temperature measurements between the static and total temperatures. Appendix B contains a detailed report on the background and experimental determination of the recovery factor.

### **3.4 Turbine Lubrication and Alignment**

Two important considerations in the rig design were turbine lubrication and turbine alignment. Under normal operation, the JetCat P-200 uses part of a fuel-oil mixture to lubricate the bearings. Since the normal fuel lines for the JetCat P-200 were removed, a separate lubrication system was necessary. From an experimentally measured flow rate of fuel-oil mixture taken by the author at WPAFB, it was determined that a maximum of 2 cc/min of oil enters the turbine. A hole in the JetCat housing normally injects the fuel-oil



Table 3.2: Calculated parameters and the measured input values.

Calculated Value	Measured Input Values
Efficiency	turbine inlet temperature turbine inlet total pressure turbine exit temperature turbine exit total pressure
Pressure Ratio	turbine inlet total pressure turbine exit total pressure
Corrected Mass Flow	sonic nozzle upstream pressure sonic nozzle upstream temperature turbine inlet temperature turbine inlet total pressure
Specific Work	sonic nozzle upstream pressure sonic nozzle upstream temperature compressor mass flow compressor inlet temperature compressor exit temperature

mixture directly into the forward bearings. After removing the original tube, which was secured using epoxy, a new tube was inserted into the hole and secured using JB Weld. A syringe pump was used to push 2 cc/min of Aeroshell 500 turbine oil through this tube into the hole that lubricates the forward bearings. The tube feeding the forward bearings is shown in Figure 3.15. A similar method was used by Tellefsen [14]. There is not, however, an opening to feed the rear bearings, so the turbine was mounted in a vertical position, which allows the oil from the forward bearings to drain down to the rear bearings.

In order to obtain the correct turbine alignment, the turbine was mounted in an extruded aluminum frame that would allow adjustment. The turbine alignment was checked by inserting a 0.006 inch feeler gage between the turbine blades and the turbine housing. This was done at 30 degree intervals around the turbine. The turbine was then rotated 90 degrees and the alignment was checked again. This process of checking turbine alignment was performed with the turbine in 4 different positions, each 90 degrees from the previous

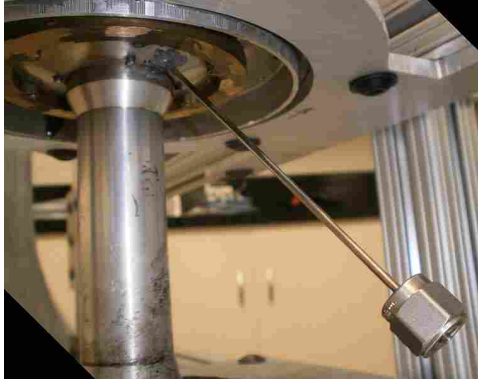


Figure 3.15: Lubrication tube, which is 2 mm in diameter.

location. Each time before beginning testing the turbine alignment was checked to prevent damage resulting from the turbine contacting the housing.

### 3.5 Testing Methodology

There were three main sets of data. The first set of data was collected with an orifice plate to measure turbine mass flow. This first set of data yielded a turbine map that did not show any differences in performance across the entire operating range. This first data set revealed some minor flaws in the rig that had resulted from unknown design values being under or over estimated. These flaws included oversized pressure transducers and a poorly located thermocouple. The correction of these flaws is discussed in the following section.

Part of addressing the flaws included installing a new supply line. The orifice plate was also upgraded to a sonic nozzle as a planned rig upgrade. Because of the sonic nozzle and new supply line, operating set points for the rig needed to be determined. This was done by incrementally closing the throttling valve and measuring the mass flow through the sonic nozzle. It was found that for a supply tank pressure of 147 psi, the 2 inch throttle gate valve needed to be set between 5.5 and 5.75 turns closed to provide the desired mass flows of 0.3 to 0.65 kg/sec to the turbine.

The second set of data was then collected at 4 different mass flow set points. This set of data yielded a steady compressor map that looked as expected, but an unusual steady turbine map. This set of data will be discussed in more detail in the next chapter. This data was used to determine the compressor peak efficiency.

For the third set of data, which is the main data presented in this thesis, the compressor was set to run at peak efficiency for reasons discussed in the next chapter. The range of desired turbine mass flows was divided into 10 set points. The rig was run at each of these 10 set points at 4 different pulsing valve motor rotation speeds, 0, 300, 600, and 1200 rpm, for a total of 40 runs. Each run was 30 seconds long to account for the response time of the thermocouples. The data was recorded for the entire 30 second interval, however, only the last 5 seconds of data was used in averaging to obtain the performance map points. A detailed procedural checklist for testing is found in Appendix C.

### **3.6 Rig Modifications**

Several modifications have been made to the initial test rig presented in a previous paper [25] to obtain the data presented in this thesis. These modifications were made because of things learned about the rig that needed to be changed or because they were planned rig upgrades. Some of the modifications are discussed elsewhere in this paper, but are mentioned in this section for the convenience of the reader.

The initial rig was only able to obtain a maximum mass flow through the turbine of 0.5 kg/sec. This limitation occurred because there was only a 1 inch pipe supply line from the large compressed air tank. Initial calculations of the flow through the pipe indicated that the 1 inch pipe line would be sufficient. However, the pressure losses due to the tees and elbows in the line were underestimated and proved to limit the flow more than previously thought. A new exit on the compressed air tank was installed with a 2 inch supply line, which increased the mass flow capability of the rig to 1.2 kg/sec. This increase in mass flow capability allowed the full rotational speed range of the JetCat turbine to be reached.

As mentioned in the Section 3.3, a sonic nozzle was used to measure the mass air flow. Previously, an orifice plate was used to measure the mass air flow. This was a planned rig upgrade. When building the rig initially, it was difficult to determine the pressure upstream of the mass flow measuring device. Because of the expense of purchasing a sonic nozzle, it was desired to be able to correctly size the sonic nozzle for the rig before spending the money. Calculations were done with Fanno flow to estimate the pressure loss through the supply line, but correlations to account for elbows and tees with compressible flow were not

found. Because the flow calculations were only estimates, an inexpensive way to validate the calculations and experimentally determine the pressure and mass flow before purchasing a sonic nozzle was desired. Therefore, an orifice plate was initially used since it is 25 times less expensive than a sonic nozzle. After verifying the pressure and mass flow, a sonic nozzle was purchased and implemented into the rig. The upgrade to the sonic nozzle allowed for a more accurate measurement of the mass air flow through the turbine.

The surge tank and bypass valve, explained in Sections 3.2 and 3.2.1, were two other modifications made to the rig. Running the pulsing valve with pulsing for the first time without the bypass valve or surge tank caused the sonic nozzle to choke and unchoke as the pulsing valve opened and closed. The surge tank was the initial solution to this problem since it would act as a capacitor and damp out the pressure pulses seen by the sonic nozzle. This solution was viable for the first few seconds of runtime, but the pressure in the tank would eventually build up and the sonic nozzle would begin to choke and unchoke with the opening and closing of the pulsing valve. The addition of the bypass valve allowed air to leak past the pulsing valve and prevented the pressure upstream of the pulsing valve from building up enough to unchoke the sonic nozzle.

Another modification was relocating the compressor exit temperature measurement thermocouple. Before, the compressor exit temperature was measured about 7 feet downstream of the compressor exit for convenience in location. However, the previous data did not yield a compressor map in keeping with established theory. As the compressor exit air was the hottest air in the rig, it was thought that heat transfer might be introducing error in the compressor exit temperature measurement. Moving the thermocouple closer to the compressor exit decreased the amount of surface area for heat transfer to occur before the compressor exit temperature was measured.

The data obtained in the first set of data used pressure transducers with a full scale of 200 psia. Because of this larger scale, they also had a large error since the pressure transducer error is based on a full scale value. It was discovered that most of the pressures measured were less than 50 psia, so those pressure transducers were switched to pressure transducers with a full scale of 50 psia. This resulted in a decreased measurement error by about a factor of 2.

## CHAPTER 4. RESULTS AND DISCUSSION

The rig was designed to use the compressor as a dynamometer for the turbine. After some initial data collection, the turbine map was not looking as expected. While considering several possible solutions to solve this problem, it was eventually noticed that in the work of Rouser *et al.* [2,11,13], who also used the compressor as a dynamometer, the compressor was set to operate at peak efficiency in the middle of the compressor map. It was concluded that for the compressor to perform adequately as a dynamometer it needed to operate near the center of the operating map. At higher mass flows the compressor pressure ratio is about 1.25. At this lower pressure ratio, the compressor does not provide adequate braking for the turbine. As the compressor efficiency increases, the compressor pressure ratio increases to between 1.5 and 2, depending on the compressor speed. For 100% operating speed, the compressor pressure ratio is 2 at compressor peak efficiency. These higher compressor pressure ratios provide more resistance for the turbine. As the compressor efficiency begins to roll over, the compressor mass flow is also decreasing, which results in a decrease in compressor work to about 60% of the peak work value. Lower work also means that the compressor is not adequately braking the turbine.

It is important to note that the compressor peak efficiency and peak work did not occur at the same point on the compressor operating map. Peak work occurred at a higher mass flow than peak efficiency. It seems reasonable that the peak work operating point could have also been chosen, but it was decided to use the same operating point as Rouser *et al.*, compressor peak efficiency. From the second set of test data, a compressor map was created and is shown in Figure 4.1. This map allowed the peak efficiency point to be determined. The turbine was then tested at different mass flows with the compressor set to operate at peak efficiency. This method only allowed one point on each speed line to be obtained for

the turbine. Thus, all of the points on the plots of turbine performance metrics presented in this chapter are each points from a different speed line.

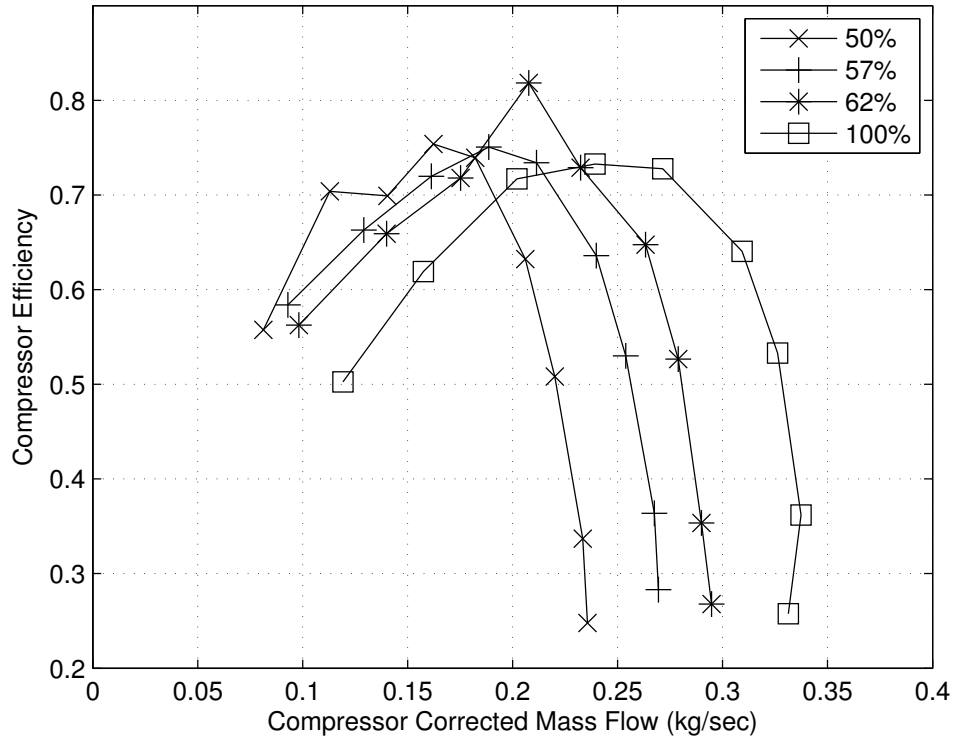


Figure 4.1: Compressor map of efficiency vs. corrected mass flow for the JetCat P-200. Percents in the legend are a percent of the maximum operating speed, 112,000 rpm.

These data were collected with the compressor control valve positioned at the compressor exit. After collecting the data, there was a conversation with WPAFB where it was suggested that placing the compressor control valve upstream of the compressor might yield better control of the turbine map and cause the compressor to act as a better dynamometer. This method has not been attempted as of the writing of this thesis, but is a planned future rig upgrade.

#### 4.1 Error Analysis

The error analysis is presented here to give the reader an idea of the error before the results are presented. The error analysis was performed using the sequential perturbation

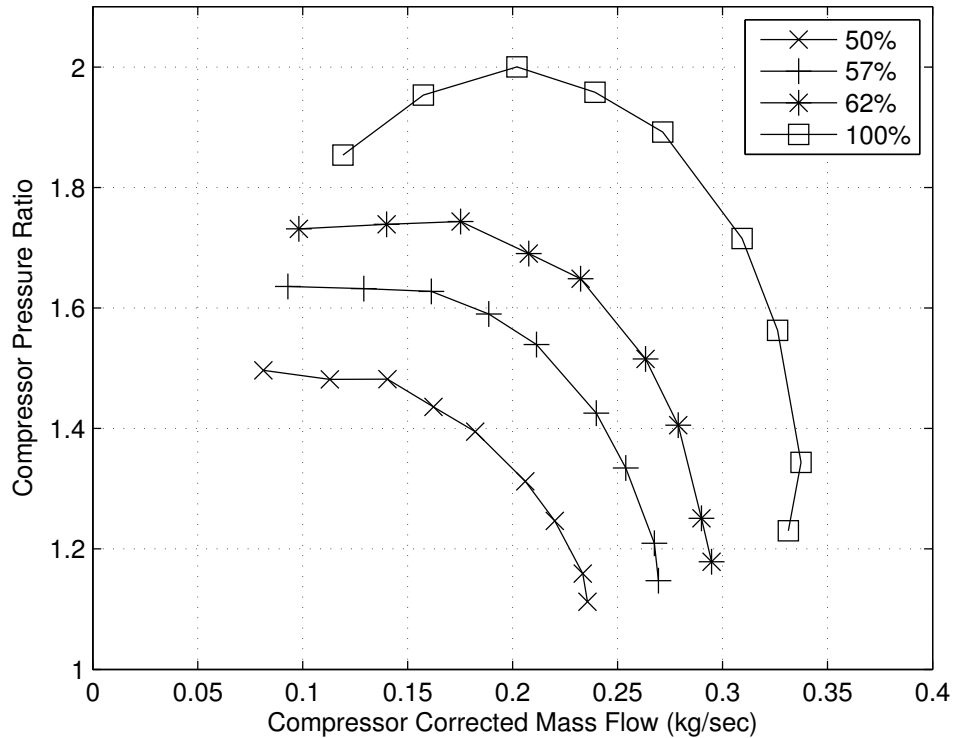


Figure 4.2: Compressor map of pressure ratio vs./ corrected mass flow for the JetCat P-200. Percents in the legend are a percent of the maximum operating speed, 112,000 rpm.

method presented by Figliola and Beasley [26] and provided in Appendix D. The values for error and percent error for the steady data are shown in Table 4.1. The error for the pulsed data is very similar to the error for the steady data, so only the steady data error is shown to provide an idea of the magnitude of the error. For the pressure ratio values, all the pulsed data errors are under 1.06%. For the efficiency values, all the pulsed data errors are below 7.5%. For the mass flow values, all the pulsed data errors are below 4.5%. Pressure ratio error, and efficiency error for the pulsed data show the same pattern as steady flow of decreasing error and percent error with increasing mass flow.

This is the first time a comparison between steady and pulsed flow has been experimentally demonstrated to this level of accuracy. Rasheed *et al.* [12] cited an efficiency error of  $\pm 8$  efficiency points, which is about 11% error. Rouser *et al.* [16] performed a sensitivity analysis for their measurement error by perturbing each measurement by 10%. This analysis showed that the exit velocity measurements were the largest source of error. They also

Table 4.1: Error and percent error for steady data.

Pressure Ratio			Efficiency			Mass Flow (kg/s)		
Value	Error	% Error	Value	Error	% Error	Value	Error	% Error
1.51	0.016	1.03	0.633	0.044	6.94	0.336	0.012	3.68
1.57	0.016	0.99	0.633	0.041	6.42	0.366	0.016	4.30
1.63	0.015	0.95	0.642	0.037	5.83	0.399	0.017	4.37
1.68	0.015	0.92	0.645	0.035	5.47	0.429	0.019	4.47
1.75	0.015	0.87	0.650	0.033	5.03	0.469	0.020	4.34
1.80	0.015	0.83	0.658	0.031	4.72	0.507	0.021	4.25
1.84	0.015	0.80	0.652	0.030	4.59	0.537	0.023	4.32
1.90	0.015	0.77	0.640	0.028	4.43	0.571	0.024	4.14
1.95	0.015	0.75	0.622	0.027	4.38	0.598	0.025	4.13
2.01	0.015	0.73	0.604	0.026	4.31	0.631	0.025	4.02

noted that the exit velocity varied by up to 16.6%, which is 1.66 times the value used in the sensitivity analysis. The sensitivity analysis yielded a turbine efficiency error of  $\pm 3.06$  efficiency points or 7.68% error. Adjusting these values to reflect the error in the exit velocity measurement yields an error of  $\pm 5.08$  efficiency points or 12.7% in turbine efficiency. This adjustment assumes a linear relationship between the measurement error and the turbine efficiency error. No error analysis was presented by St. George *et al.* for their experiment [17].

The error in the present data is approximately half the error for previous comparisons between steady and pulsed flow through an axial turbine. Rouser *et al.* [16] used a radial turbine and only tested at one operating point, so it is difficult to make a quantitative comparison with their data. Also, a linear relation assumption was made to determine the actual error in turbine efficiency from their presented sensitivity analysis. However, it is clear that the error of the data in this thesis is at least on par, and at best half of, the error found by Rouser *et al.* [16] Compared with the work of Rasheed *et al.* [12], the error of the data in this thesis is about half at worst and a third at best. The main reason for the increase in efficiency over other research is more sensitive instrumentation. Previous researchers designed their rigs to handle actual detonations, which caused a harsher environment. Thus, it was necessary to use instrumentation that was tolerant to a high temperature environment. Cold flow allows the use of more sensitive instrumentation that is less temperature tolerant.



The error in this thesis is an improvement from the first rig built and tested [25], and was made possible by pressure transducers with a full scale more tightly fitted to the values being measured as discussed in Section 3.6. The pressure ratio error is only dependent on the pressure transducer error, but the efficiency is dependent on both thermocouple and pressure transducer error. A sensitivity analysis showed that the efficiency is equally sensitive to both the temperature and pressure error.

## 4.2 Repeatability Analysis

In addition to an error analysis, data at the same operating point from three different days was used to statistically determine the repeatability error. The repeatability error was determined using the Student's t-distribution. There were 2 degrees of freedom and a confidence interval of 95%. A comparison of the instrumentation and repeatability error is shown in Table 4.2.

Table 4.2: Instrumentation and repeatability error. The repeatability error is a 95% confidence interval.

	<b>Instrumentation Error</b>	<b>Repeatability Error</b>
Efficiency	0.045	0.012
Pressure Ratio	0.016	0.011
Mass Flow (kg/sec)	0.012	0.011

The repeatability analysis shows that the repeatability of both the pressure ratio and mass flow is approximately the same as the instrumentation error. However, the repeatability of the turbine efficiency is about 0.25 times the instrumentation error. This analysis shows that the results obtained with the test rig are repeatable.

## 4.3 Steady Flow Results

The turbine steady flow results are shown in Figure 4.3, where corrected mass flow is plotted against the pressure ratio. The advantage of plotting corrected mass flow vs.

pressure ratio is that all of the data collapses onto a single curve [27]. This curve shows that the turbine is operating as expected without having to generate separate speed lines. One important thing to note about this figure is that the range of corrected mass flow is fairly small. Due to budget restraints, only a sonic nozzle for the higher mass flows was purchased. Thus, the turbine was only tested in the region close to choking, which is where the operating point normally is anyway.

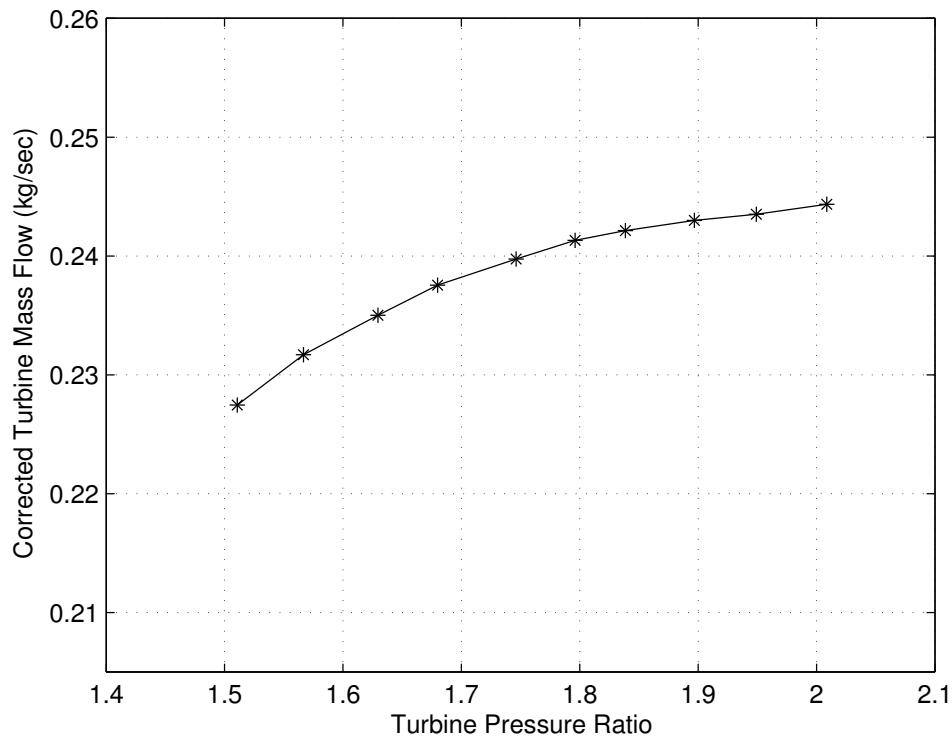


Figure 4.3: Corrected mass flow vs. pressure ratio for steady flow.

Because the JetCat is a hobbyist engine, no data on the design operating condition or the corrected conditions for the turbine was found. However, limited experimental data collected at WPAFB with the JetCat running in normal operation was available. When these experimental measurements were made on the JetCat, only the compressor mass air flow, fuel flow, rotor speed, and exhaust gas temperature were measured. The turbine inlet and exit quantities were not measured due to time restraints and space limitations within the JetCat, so direct calculation of the turbine corrected conditions was not possible. However, a model

was created using the measured values and the non-ideal gas turbine cycle equations [27] to determine approximate values for the turbine inlet and exit conditions. The measured values used in the model were compressor mass air flow, fuel flow, and exhaust gas temperature. Parameters such as the compressor pressure ratio, component efficiencies, and turbine exit pressure were assumed. Because many values were assumed, the model can only be used as a general guideline and comparisons made with the model should be conducted with caution. With this in mind, a comparison between the mathematical model parameters and the data from this thesis is shown in Table 4.3 and the equations for corrected mass flow and corrected speed are shown in Equations 4.1 and 4.2, respectively.

Table 4.3: JetCat mathematical model compared with the data for this thesis.

Quantity	JetCat Model		Cold Flow Data	
	Max	Min	Max	Min
Turbine Pressure Ratio	2.3	1.7	2.0	1.5
Corrected Mass Flow (kg/sec)	0.24	0.09	0.24	0.23
Corrected Speed (rpm)	55717	18520	119300	56420

$$\dot{m}_c = \frac{\dot{m} \sqrt{T_{0i}/T_{stp}}}{p_{0i}/p_{stp}} \quad (4.1)$$

$$N_c = \frac{N}{\sqrt{T_{0i}/T_{stp}}} \quad (4.2)$$

The pressure ratio range compares well with the model. The corrected mass flow is on the higher end compared with the model, but this is to be expected, since, as discussed above, only the higher mass flows were tested for this paper. The main discrepancies with the model lie in the corrected speed. This was expected since cold flow was used to drive the turbine. In a larger turbine blow-down facility the air would be heated before entering the turbine, but was not feasible in this case. As shown in Equation 4.2, a higher turbine inlet temperature decreases the corrected speed. Thus, the values for corrected speed are consistent with how the rig is being operated because a higher corrected speed is expected with a lower inlet

temperature. While the measured values do not match exactly with the JetCat Model, they demonstrate that the turbine is operating near its normal operating point. A complete match of corrected conditions is not necessary because the turbine operation is not being characterized, but rather a comparison is being developed between steady and pulsed flow. Since the turbine performance is being evaluated for both steady and pulsed flow under the current operating conditions, a comparison can be made without having to perfectly match the normal corrected operating conditions.

#### 4.4 Procedure for Averaging Pulsed Flow

Different averaging techniques were considered to analyze the pulsed flow data. According to the work of Cumpsty and Horlock [21] described in Chapter 2, it is important to select an averaging method to preserve information about the quantities of interest. For this thesis, the quantities of interest were the turbine mass flow, turbine work, turbine pressure ratio, and turbine efficiency. Thus, the most appropriate averaging method would be a work average since it preserves these quantities. The work averaging method presented by Suresh *et al.* [23] was the most detailed and applicable to the work of this thesis and so it was chosen for the averaging method. Their averaging method is presented in Equations 2.6-2.9, but is also presented here for the convenience of the reader.

$$T_0^a = \frac{\int_0^\tau \rho u T_0 d\xi}{\int_0^\tau \rho u d\xi} \quad (4.3)$$

$$(p_{0i}^{wa})^{(\gamma-1)/\gamma} = \frac{\int_0^\tau \rho_i u_i T_{0i}(\xi) d\xi}{\int_0^\tau \rho_i u_i \left( \frac{T_{0i}(\xi)}{p_{0i}(\xi)^{(\gamma-1)/\gamma}} \right) d\xi} \quad (4.4)$$

$$(p_{0e}^{wa})^{(\gamma-1)/\gamma} = \frac{1}{\tau} \int_0^\tau p_{0e}^{(\gamma-1)/\gamma}(\xi) d\xi \quad (4.5)$$

$$\eta^{wa} = \frac{T_{0i}^a - T_{0e}^a}{T_{0i}^a (1 - (p_{0e}^{wa}/p_{0i}^{wa})^{(\gamma-1)/\gamma})} \quad (4.6)$$

It was decided to average over 5 seconds of data to account for any random error. As discussed in Chapter 3, there were 30 seconds of data from each run. The 5 seconds of data used in the averaging procedure were the last 5 seconds from each individual run. The integrals were numerically evaluated over the 5 second period using the time input from the data acquisition system. The averaged values were then used to calculate efficiency (Equation 4.6) and the other turbine performance parameters.

#### 4.5 Pulsed Flow Results

One of the observations made from the pulsing flow data is that the amplitude of the pressure pulses increased for higher mass flows. The amplitude also increased with decreasing pulsing frequency. The amplitude of the pressure pulses for the tested mass flows are shown in Table 4.4. Higher amplitudes for lower frequencies occur because there is a longer period for the pressure to build up behind the valve. The increase in amplitude with the increase in mass flow occurs because the bypass valve lets air past the pulsing valve, but it is set to only allow a minimal amount of air through. While not experimentally validated, it is expected that the flow is choked through the bypass valve. As the overall mass flow increases, the percentage of air going through the bypass valve compared with the pulsing valve decreases. This creates a higher pressure buildup behind the pulsing valve, and, therefore, a higher pressure amplitude as the pulsing valve opens and closes.

Figure 4.4 shows the corrected mass flow and pressure ratio for the pulsing and steady results. The curves for pulsing flow are very similar to the steady curve in both shape and magnitude. The difference between the curves is greater at lower mass flows and lower pressure ratios. It is important to note that as the pulsing frequency increases, the result comes closer to the steady data. For a pulsing frequency of 10 Hz, the turbine pressure ratio is, on average, 0.14 greater than the steady turbine pressure ratio. For 20 Hz it is 0.12 greater and for 40 Hz it is only 0.06 greater. This phenomenon is reasonable when considered with respect to a limit. As the pulsing frequency approaches infinity, it becomes more like a steady flow. This same pattern is observed in all of the following plots comparing pulsed and steady flow.

Table 4.4: Pressure pulse amplitude  
(in kPa) for tested mass  
flows (in kg/sec).

Mass Flow	10 Hz	20 Hz	40 Hz
0.34	17.7	10.1	4.8
0.38	17.7	10.1	5.1
0.41	19.7	10.0	5.4
0.44	21.7	11.0	6.1
0.47	23.1	12.0	6.6
0.51	25.5	12.7	6.8
0.54	27.2	13.7	7.7
0.57	29.0	14.8	7.8
0.60	30.8	15.2	8.3
0.64	32.5	16.7	9.1

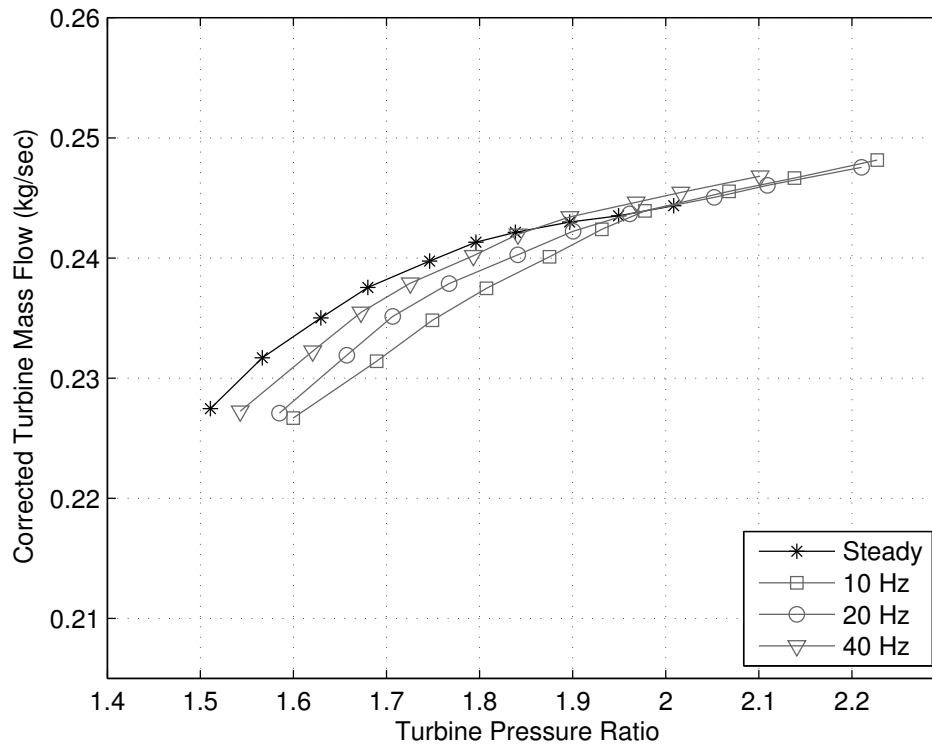


Figure 4.4: Corrected mass flow vs. pressure ratio for steady flow and various pulsed flow frequencies.

Comparing the data in this paper to the results of other researchers gives insight into how a turbine responds to different types of pulsed flow. Previous research performed by St. George *et al.* [17] on an axial turbine with cold pulsing flow used a counter-clockwise sequential firing pattern instead of a full annular pulse. Their results showed curves for corrected turbine mass flow that were concave up instead of concave down and were shifted down and to the right of the steady curve. The results they obtained were closer to a partial admission driven turbine. In Figure 4.4, the data in this paper shows that the pulsed corrected mass flow vs. pressure ratio curves are similar to the steady flow curve. The reason for this is the full annular pulse used to drive the turbine in this paper compared with the partial admission pulsed used by St. George *et al.* to drive their turbine. A full admission turbine has a higher mass flow than a turbine driven by a sequential firing pattern and, therefore, would have curves more similar to the full admission steady flow driven turbine.

The efficiency plot in Figure 4.5 shows the difference in efficiency between the steady and pulsed flow. Turbine efficiency is the main point of comparison between steady and pulsed flow. It was found that the peak efficiency dropped 5.6 efficiency points from steady flow efficiency for 40 Hz, 9.4 efficiency points for 20 Hz, and 11.7 efficiency points for 10 Hz. When looking at the turbine efficiency map, remember that each of the points on a given curve are from different speed lines. This means that the data is essentially walking across the efficiency islands on the turbine map. This concept is illustrated in Figure 4.6 where the data is taken along the line labeled “Data Line.” Taking data in this manner yields the curve shape seen in Figure 4.5 where the efficiency increases to a peak efficiency and then decreases. Another interesting feature of Figure 4.5 is that the peak efficiency shifts to higher pressure ratios with decreasing pulsing frequency.

Not only are the efficiency results reasonable, they also compare well with the experimental results of other researchers where the turbine is closely coupled with the pressure pulses. Rouser *et al.* [16] found a drop of about 20 efficiency points for a radial turbine with a pulsing frequency of 30 Hz. St. George *et al.* [17] found a drop of about 15 points in peak efficiency for pulsing flow with a frequency between 5 and 20 Hz. It is difficult to make a direct comparison in efficiency with these other researchers because Rouser *et al.* used a radial turbine and St. George *et al.* used an axial turbine with a different geometry and

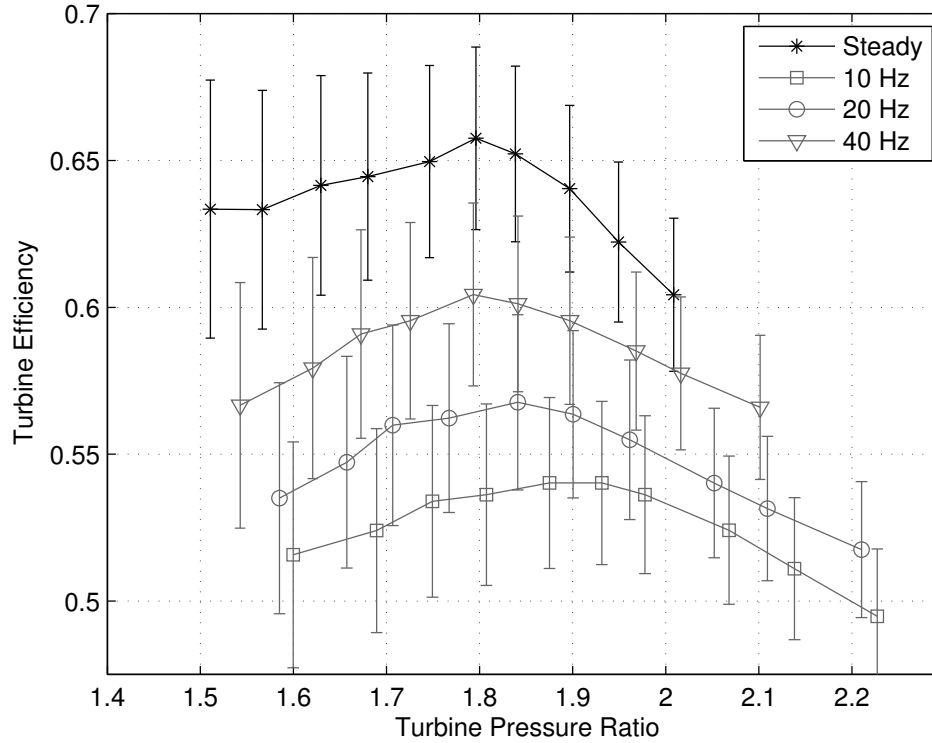


Figure 4.5: Turbine efficiency vs. pressure ratio for steady flow and various pulsed flow frequencies. The error bars reflect the instrumentation error. Recall that the repeatability is about 0.25 times the instrumentation error.

a lower pressure ratio than the one used in this paper. However, a tentative comparison between the data from this paper and the data of St. George *et al.* shows that the efficiency drop from pulsing flow is less for full annular flow than for a pulsing pattern where there are some inactive sectors. The larger drop in efficiency for a sequential firing configuration occurs because the turbine is only being driven by one sector at a time. The drop in efficiency obtained by Rouser *et al.* [16] is larger because they used an actual detonation, which has a much larger amplitude, to drive the turbine. This larger pressure amplitude means that the turbine is operating off-design for more of the cycle, yielding a larger drop in efficiency. Also, they used a radial turbine, which will respond differently than an axial turbine to pressure pulses.

A numerical study of turbine performance under pulsed flow was recently presented by Ni *et al.* [19]. They showed that a turbine driven by full admission pulses was more efficient than a turbine driven by partial admission pulses, which supports the findings presented



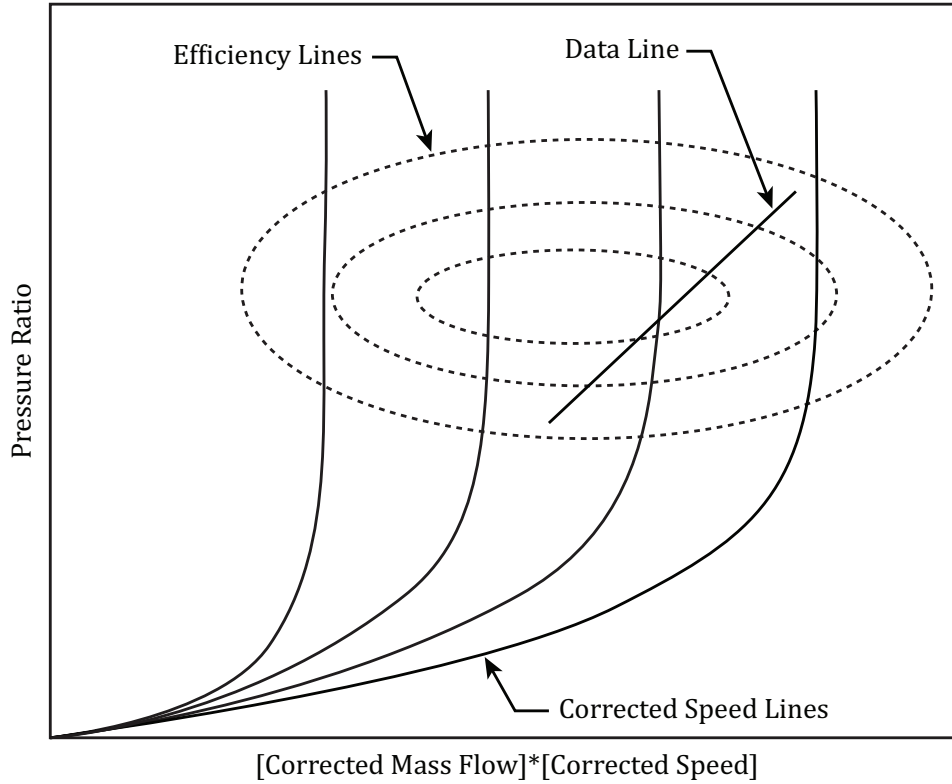


Figure 4.6: Standard turbine map showing how data was collected. The x-axis is corrected mass flow multiplied by corrected speed and the y-axis is total pressure ratio. The data for this paper was collected on the line indicated by “Data Line.”

in the preceding paragraph. However, they also found that the efficiency decreases as the pulsing frequency increases, which is contradictory with the data presented in this thesis. One explanation for this is the duty cycle of the pulse. They used a pulse with a shape close to a step function with a duty cycle of 30%. In these experiments, as well as the experiments of Rouser *et al.* [16] and St. George *et al.* [17], the shape of the pulse is closer to a sinusoid since the opening and closing of the valves is not instantaneous. Because Ni *et al.* used a pressure pulse with such a low duty cycle, there are relatively large periods of no flow. At higher frequencies, the short periods of flow are unable to adequately accelerate the turbine to a state that could be achieved with a pulse with a higher duty cycle.

The specific power for the turbine is plotted in Figure 4.7. This figure shows that the specific power increases as the pulsing frequency is increased. A similar result was also

found by Rouser *et al.* [16] and St. George *et al.* [17]. The opposite result was presented by Ni *et al.* [19]. However, the same explanation as was given in the previous paragraph for efficiency also applies to the specific power. Our data shows that, on average, for a given pressure ratio, the specific power is 1.91 kJ/kg lower for pulsed flow at 10 Hz, 1.40 kJ/kg lower for 20 Hz, and 0.43 kJ/kg lower for 40 Hz.

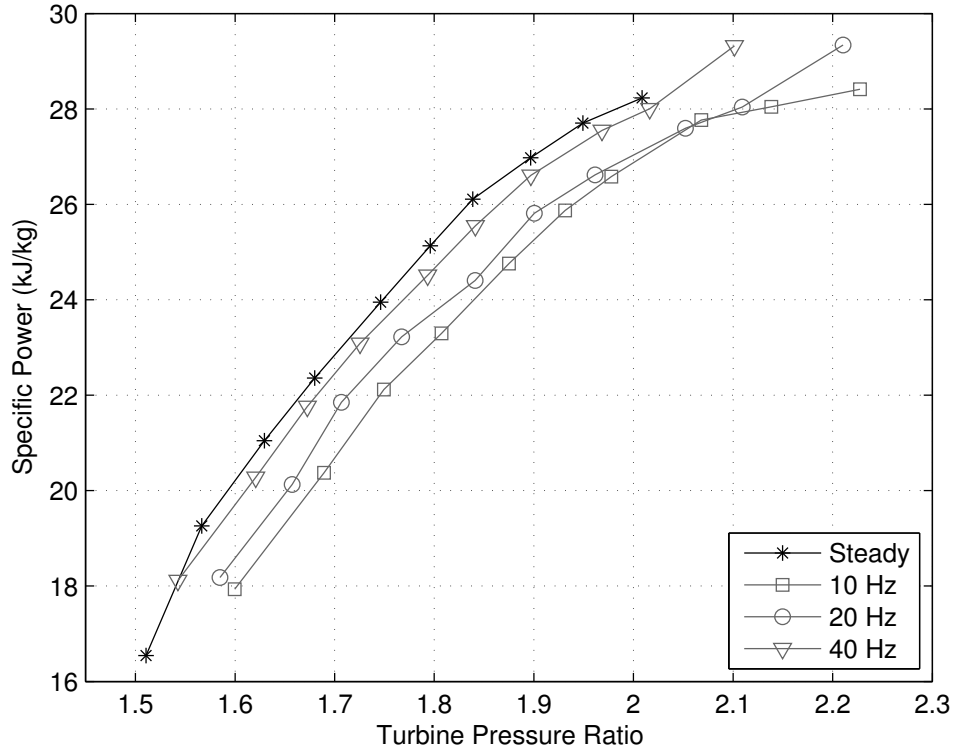


Figure 4.7: Specific work vs. pressure ratio for steady flow and various pulsed flow frequencies.

#### 4.6 Physical Explanation of Results

There are two main trends observed in the data. First, the performance of a turbine driven by pulsed flow is lower than when the turbine is driven by steady flow. Second, the turbine performance under pulsed flow conditions increases as the pulsing frequency increases. The first trend can be explained by the unsteadiness of the flow. Given a turbine mass flow, there is an optimum pressure ratio and turbine speed for maximum turbine performance. However, with pulsing flow the pressure ratio and turbine speed are constantly

changing. Even though the turbine might operate on-design for a small time during the pulsing cycle, it is operating off-design for most of the cycle. Because of this, it is expected that turbine performance will be lower when driven with pulsed flow.

The expected decrease in turbine performance might seem in contradiction with previous statements in this thesis that integrating PDEs into GTEs can increase performance. It is not a contradiction, but a trade-off. The turbine performance is expected to decrease. However, performance gains will be made from the pressure gain combustion and burning the fuel in bursts instead of constantly. These gains are estimated to be great enough to overcome the decrease in turbine performance. Rasheed *et al.* [12] experimentally demonstrated this increase with a 4% increase in rig efficiency when using PDEs to drive a turbine. While there are gains from using a PDE in place of a regular combustor, this thesis focused on turbine performance under pulsed flow and did not consider the overall performance. The question for future work is how to minimize the drop in turbine efficiency so that the overall performance gain will be greater.

The second trend of increasing turbine performance with increasing pulsing frequency can be explained both with limit theory and pulsing amplitude. As mentioned in Section 4.5, as the frequency increases the pulse becomes more like steady flow in the limit. Because of the inertia associated with the air, it is more difficult for the air to change pressure and the high frequency pressure pulses are dampened by the inertia of the air.

The amplitude of the pressure pulse also explains the second trend. When the pulsing valve is opening and closing at a higher frequency, there is less time for pressure to build up behind the valve before it is released. Since the pressure behind the valve is released more frequently, there are smaller fluctuations in pressure. This effect is seen in Table 4.4 where higher pulsing frequencies have a smaller pulsing amplitude.

## CHAPTER 5. CONCLUSIONS

Experiments with pulsed flow driven axial turbine performance prior to 2013 did not show any significant difference in turbine performance from steady state since the pressure pulses were loosely coupled with the turbine. This is the first work to compare steady flow through an axial turbine with full annular pulsed flow closely coupled with the turbine. The data shows that a turbine driven by full annular pressure pulses has operation curves that are similar in shape to steady state operation curves, but with a decrease in turbine performance that is dependent on pulsing frequency.

- It was demonstrated that the turbine pressure ratio increases with pulsed flow through the turbine and that this increase is less for higher pulsing frequencies. For 40 Hz operation the turbine pressure ratio increases by 0.06, for 20 Hz it increases by 0.12, and for 10 Hz it increases by 0.14.
- It was demonstrated that the peak efficiency is lower for pulsed flow when compared with steady flow. The difference between steady and pulsed flow is less severe at higher pulsing frequencies. For 40 Hz operation the turbine efficiency decreases by 5 efficiency points, for 20 Hz it decreases by 9 points, and for 10 Hz it decreases by 11 points.
- It was demonstrated that the specific power at a given pressure ratio for pulsed flow is lower than that of steady flow and that the decrease in specific power is lower for higher pulsing frequencies. On average, the difference in specific power between steady and pulsed flow is 0.43 kJ/kg for 40 Hz, 1.40 kJ/kg for 20 Hz, and 1.91 kJ/kg for 10 Hz.
- It was demonstrated that the error in these data is approximately half of the error in similar previous studies.

## 5.1 Future Work

This thesis compared performance of an axial turbine driven by steady flow and full annular pulsed flow. A next step would be to obtain results for partial admission pulsed flow and compare that with the full admission pulsed flow. Other literature has compared partial admission pulsed flow with steady flow, but has not established a relation between the full and partial admission pulsed flow. Previous work has not been able to generate full admission pulsed flow due to rig limitations. Since this work has already generated data for full admission pulsed flow, this gap can be bridged by collecting data on partial admission pulsed flow.

Another area of investigation is to compare steady flow, full admission pulsing flow, and partial admission pulsing flow without the bypass valve. In this thesis the bypass valve was used to prevent the sonic nozzle from unchoking so that an accurate measure of the mass flow could be made. Without the bypass valve, the sonic nozzle would unchoke and yield the mass flow measurement inaccurate. However, without the bypass valve, the pressure pulses would have a greater amplitude. The difficulty for this study is accurately measuring the mass flow.

Performing these two areas of research will help to further understand the effect of pulsing flow on turbine performance.

## REFERENCES

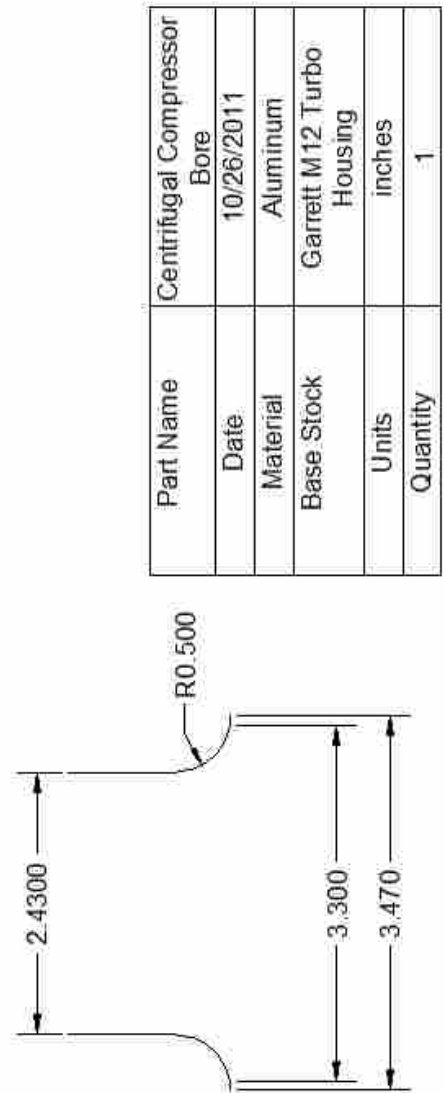
- [1] L. Barr, “Pulsed detonation engine flies into history,” May 2008. [Online]. Available: [www.afmc.af.mil/news](http://www.afmc.af.mil/news) 1
- [2] K. P. Rouser, P. I. King, F. R. Schauer, R. Sondergaard, and J. L. Hoke, “Performance evaluation of an unsteady turbine driven by a pulsed detonation combustor,” in *Proceedings of ASME Turbo Expo 2011*, Vancouver, British Columbia, Canada, 2011, GT2011-45396. 2, 4, 9, 35
- [3] A. J. Dean, A. Rasheed, V. Tangirala, and P. F. Pinard, “Operation and noise transmission of an axial turbine driven by a pulse detonation combustor,” in *Proceedings of the ASME Turbo Expo 2005: Power for Land, Sea and Air*, Reno, Nevada, 2005, GT2005-69141. 2
- [4] M. A. Mawid, T. W. Park, B. Sekar, and C. Arana, “Application of pulse detonation combustion to turbofan engines,” *Journal of Engineering for Gas Turbines and Power*, vol. 125, no. 1, pp. 270–283, 2003. 3
- [5] D. P. Petters and J. L. Felder, “Engine system performance of pulse detonation concepts using the npss program,” in *38th AIAA/ASME/SAE/ASEE Joint Propulsion Conference and Exhibit*, Indianapolis, Indiana, 2002, AIAA 2002-3910. 3
- [6] A. J. Glaser, N. Caldwell, and E. Gutmark, “Performance of an axial flow turbine driven by multiple pulse detonation combustors,” in *45th AIAA Aerospace Sciences Meeting and Exhibit*, Reno, Nevada, 2007, AIAA 2007-1244. 3, 4, 8, 9, 10, 62, 63
- [7] D. C. Hofer, V. E. Tangirala, and A. Suresh, “Performance metrics for pulse detonation combustor turbine hybrid systems,” in *47th AIAA Aerospace Sciences Meeting Including the New Horizons Forum and Aerospace Exposition*, Orlando, Florida, 2009, AIAA 2009-292. 3, 4
- [8] F. Schauer, R. Bradley, and J. Hoke, “Interaction of a pulsed detonation engine with a turbine,” in *41st AIAA Aerospace Sciences Meeting and Exhibit*, Reno, Nevada, 2003, AIAA 2003-0891. 4, 7
- [9] A. Rasheed, V. E. Tangirala, C. L. Vadervort, and A. J. Dean, “Interactions of a pulsed detonation engine with a 2d blade cascade,” in *42nd Aerospace Sciences Meeting and Exhibit*, Reno, Nevada, 2004, AIAA 2004-1207. 4, 7
- [10] A. Rasheed, A. Furman, and A. Dean, “Experimental investigations of an axial turbine driven by a multi-tube pulsed detonation combustor system,” in *41st AIAA/ASME/SAE/ASEE Joint Propulsion Conference and Exhibit*, Tucson, Arizona, 2005, AIAA 2005-4209. 4, 8, 9

- [11] K. P. Rouser, P. I. King, F. R. Schauer, R. Sondergaard, and J. L. Hoke, “Unsteady performance of a turbine driven by a pulse detonation engine,” in *48th AIAA Aerospace Sciences Meeting Including the New Horizons Forum and Aerospace Exposition*, Orlando, Florida, 2010, AIAA 2010-1116. 4, 9, 35
- [12] A. Rasheed, A. H. Furman, and A. J. Dean, “Experimental investigations of the performance of a multitube pulse detonation turbine system,” *Journal of Propulsion and Power*, vol. 27, no. 3, pp. 586–596, 2011. 4, 8, 9, 37, 38, 49, 62, 63
- [13] K. P. Rouser, P. I. King, F. R. Schauer, R. Sondergaard, L. P. Goss, and J. L. Hoke, “Time-accurate flow field and rotor speed measurements of a pulsed detonation driven turbine,” in *49th AIAA Aerospace Sciences Meeting including the New Horizons Forum and Aerospace Exposition*, Orlando, Florida, 2011, AIAA 2011-577. 4, 9, 35
- [14] J. Tellefsen, “Build up and operation of an axial turbine driven by a rotary detonation engine,” Masters Thesis, Air Force Institute of Technology, 2012. 4, 27, 31, 62, 63
- [15] A. C. St. George and E. J. Gutmark, “Trends in pulsating turbine performance: Pulse-detonation driven axial flow turbine,” in *50th AIAA Aerospace Sciences Meeting including the New Horizons Forum and Aerospace Exposition*, Nashville, Tennessee, 2012, AIAA 2012-0769. 4
- [16] K. P. Rouser, P. I. King, F. R. Schauer, R. Sondergaard, and J. L. Hoke, “Experimental performance evaluation of a turbine driven by pulsed detonations,” in *51st AIAA Aerospace Sciences Meeting including the New Horizons Forum and Aerospace Exposition*, Grapevine, Texas, 2013, AIAA 2013-1212. 4, 9, 14, 15, 37, 38, 45, 46, 47, 48
- [17] A. St. George, R. Driscoll, D. Munday, and E. J. Gutmark, “Experimental investigation of axial turbine performance driven by steady and pulsating flows,” in *51st AIAA Aerospace Sciences Meeting including the New Horizons Forum and Aerospace Exposition*, Grapevine, Texas, 2013, AIAA 2013-0276. 4, 9, 38, 45, 47, 48
- [18] D. Munday, A. S. George, R. Driscoll, W. Stoddard, B. Romanchuk, and E. Gutmark, “The design and validation of a pulse detonation engine facility with and without axial turbine integration,” in *51st AIAA Aerospace Sciences Meeting including the New Horizons Forum and Aerospace Exposition*, Grapevine, Texas, 2013, AIAA 2013-0275. 4, 9, 62, 63
- [19] R. H. Ni, W. Humber, M. Ni, R. Sondergaard, and M. Ooten, “Performance estimation of a turbine under partial-admission and flow pulsation conditions at inlet,” in *Proceedings of ASME Turbo Expo 2013: Turbine Technical Conference and Exposition*, San Antonio, Texas, 2013, GT2013-94811. 4, 10, 15, 46, 48
- [20] T. E. Hutchins and M. Metghalchi, “Energy and exergy analyses of the pulse detonation engine,” *Journal of Engineering for Gas Turbines and Power*, vol. 125, no. 4, pp. 1075–1080, 2003. 6
- [21] N. A. Cumpsty and J. H. Horlock, “Averaging nonuniform flow for a purpose,” *Journal of Turbomachinery*, vol. 128, no. 1, pp. 120–129, 2006. 11, 13, 16, 42

- [22] A. Nango, K. Inaba, T. Kojima, and M. Yamamoto, “Numerical study on single-stage axial turbine with pulse detonation combustor,” in *47th AIAA Aerospace Sciences Meeting including the New Horizons Forum and Aerospace Exposition*, Orlando, Florida, 2009, AIAA 2009-294. 12
- [23] A. Suresh, D. C. Hofer, and V. E. Tangirala, “Turbine efficiency for unsteady, periodic flows,” *Journal of Turbomachinery*, vol. 134, no. 3, 2012. 12, 13, 16, 42
- [24] “Jetcat usa.” [Online]. Available: <http://www.jetcatusa.com/p200.html> 17
- [25] M. H. Fernelius, S. E. Gorrell, J. L. Hoke, and F. R. Schauer, “Design and fabrication of an experimental test facility to compare the performance of pulsed and steady flow through a turbine,” in *51st AIAA Aerospace Sciences Meeting including the New Horizons Forum and Aerospace Exposition*, Grapevine, Texas, 2013, AIAA 2013-0277. 33, 39, 62, 63
- [26] R. S. Figliola and D. E. Beasley, *Theory and Design for Mechanical Measurements*, 4th ed. John Wiley & Sons, Inc., 2006. 37, 62, 69, 73, 79
- [27] R. D. Flack, *Fundamentals of Jet Propulsion with Applications*. New York: Cambridge University Press, 2005. 40, 41, 62
- [28] J. E. John and T. G. Keith, *Gas Dynamics*, 3rd ed. Upper Saddle River, New Jersey: Pearson Prentice Hall, 2006. 62, 65
- [29] G. Paniagua, R. Denos, and M. Oropesa, “Thermocouple probes for accurate temperature measurements in short duration facilities,” in *Proceedings of ASME Turbo Expo 2002*. Amsterdam, The Netherlands: ASME, Jun. 2002. GT2002-30043. 63, 66, 73



APPENDIX A. PART DRAWINGS



Part Name	Centrifugal Compressor Bore
Date	10/26/2011
Material	Aluminum
Base Stock	Garrett M12 Turbo Housing
Units	inches
Quantity	1

Figure A.1: Drawing of the compressor bore. Courtesy of Jonathan Tellefsen.

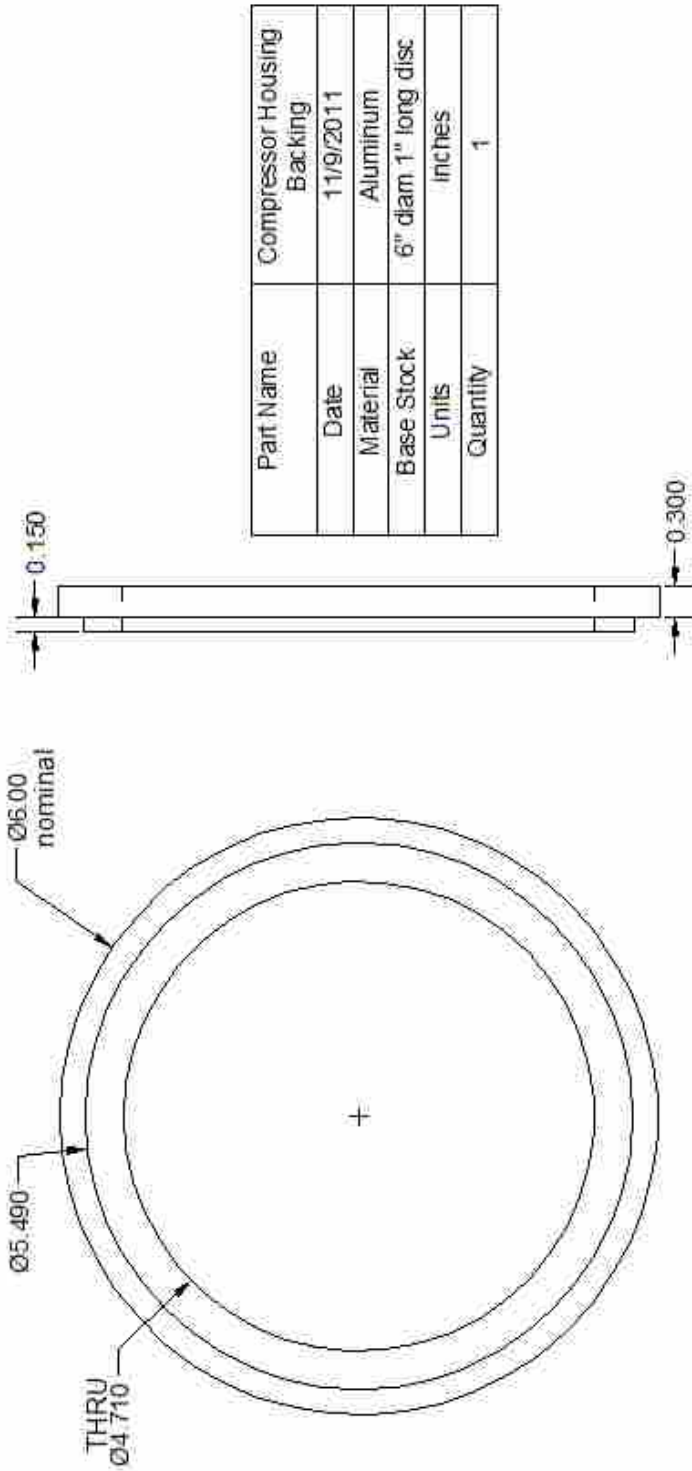
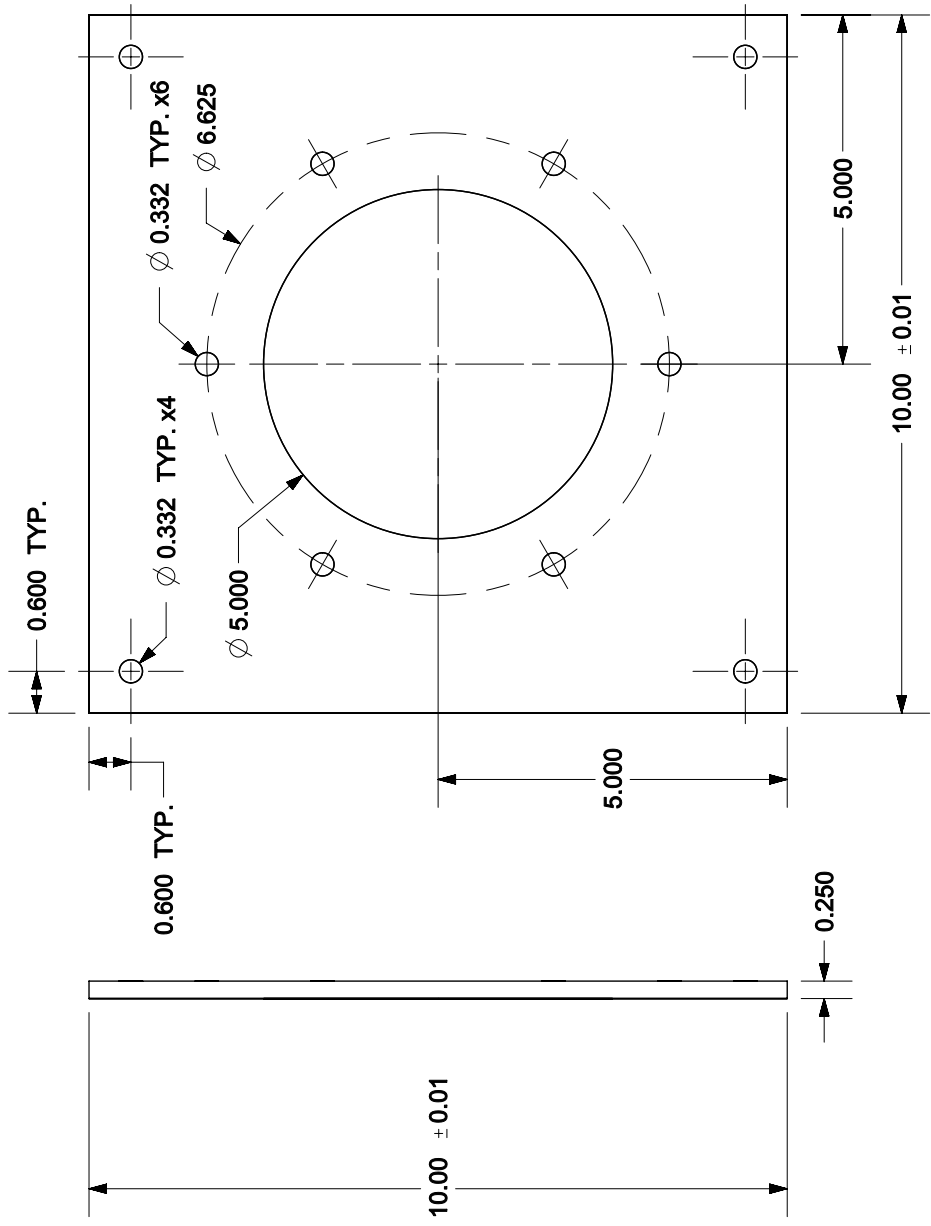


Figure A.2: Drawing of the compressor backing. Courtesy of Jonathan Tellefsen.



Designer	Joshua Wilson
Drafter	Mark Fernelius
Part Name	Compressor Plate
Dimensions	inches
Tolerances	± 0.005 unless otherwise specified

Figure A.3: Plate to attach the compressor housing to the test rig frame.

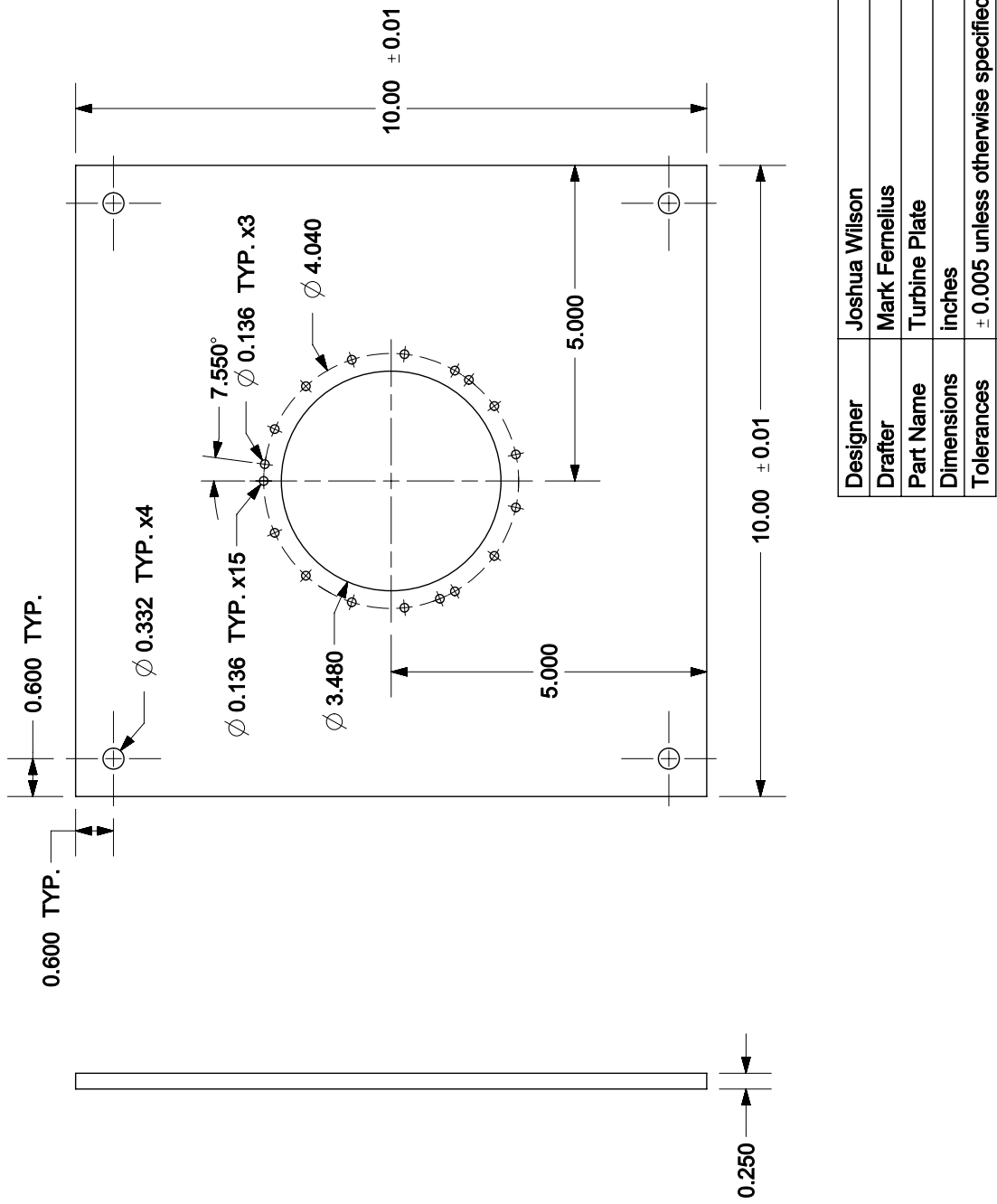


Figure A.4: Plate to attach the turbine housing to the test rig frame.

Attaching the motor to the ball valve required modification of the valve stem. The valve handle was removed and a new valve stem was made that would allow the motor to be attached to the ball valve with a coupler. This ball valve to coupling converter is shown in Figure A.5. The ball valve to coupling converter was not well supported with the original ball valve packing nut, which caused friction and visible wear on the ball valve to coupling converter. A brass sleeve bearing was manufactured for the ball valve to coupling converter to provide a better bearing surface. Ken Forster of the BYU Mechanical Engineering machine shop manufactured this piece based on the needs and the dimensions of the original ball valve packing nut. No drawing or part model was made before the part was manufactured. Images of the original ball valve packing nut and the new bearing are shown in Figure A.6. The coupler was a multi-flex shaft coupling with a rubber element to account for slight misalignment.

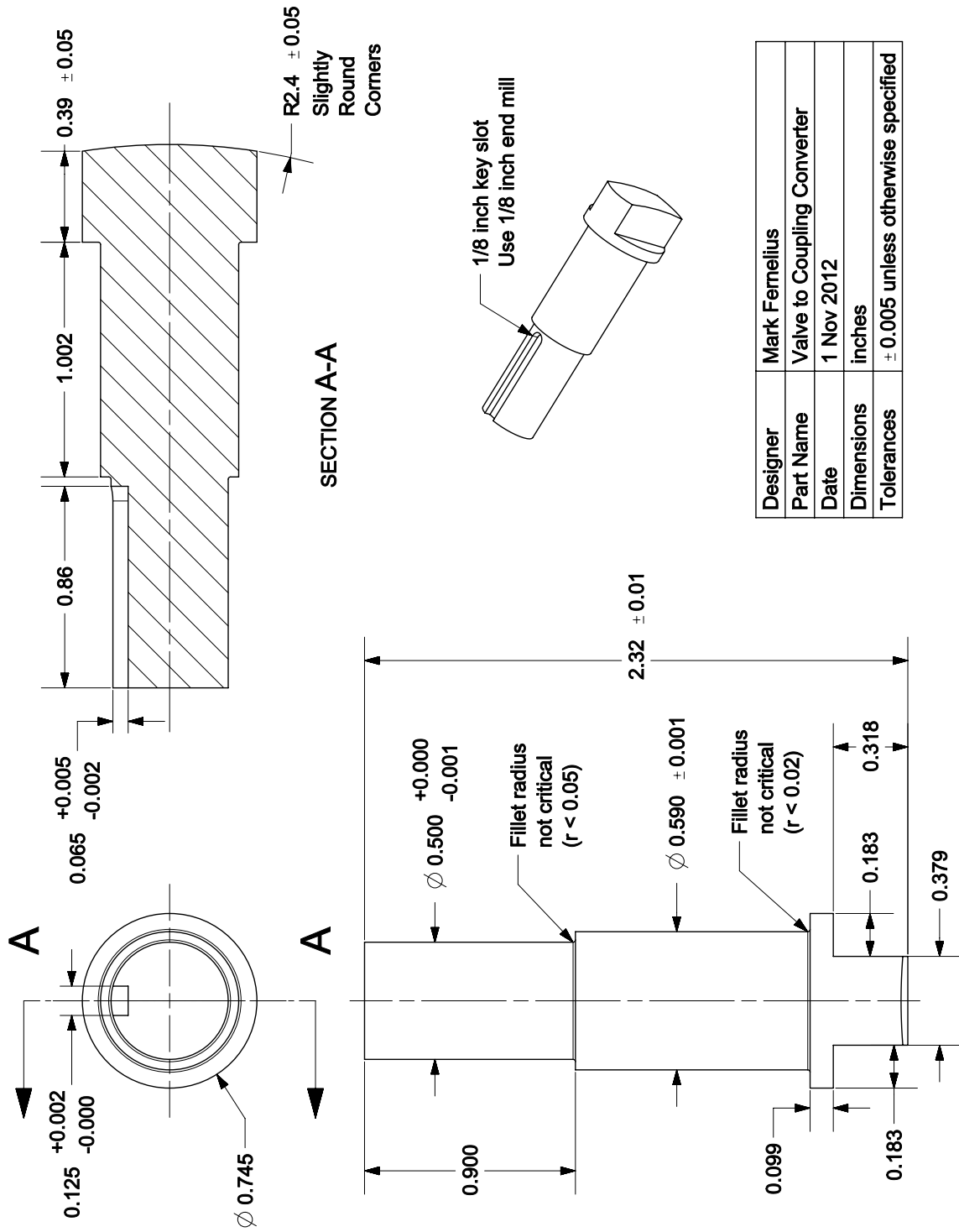
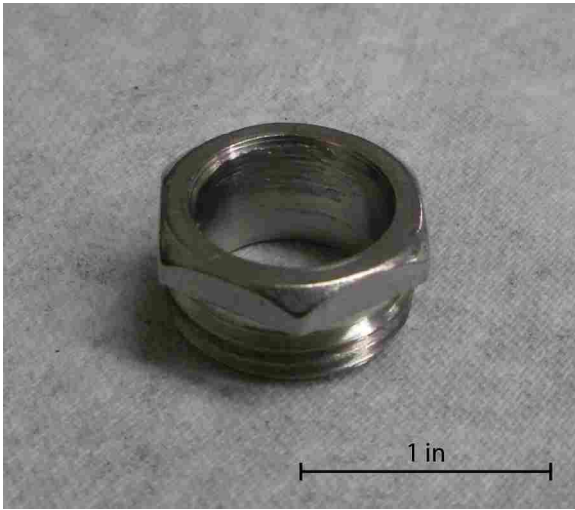


Figure A.5: Ball valve to coupling converter.



(a) Original ball valve packing nut.



(b) Ball valve stem bearing.

Figure A.6: Ball valve packing nut and bearing.



Figure A.7: Ball valve parts for test rig.

## APPENDIX B. THERMOCOUPLE RECOVERY FACTOR

### B.1 Introduction

Thermocouples are often used to measure the temperature of the working fluid in turbomachinery applications [6, 12, 14, 18, 25]. Because the calculation of turbomachinery performance parameters are based on the temperatures before and after the different components [27], it is important that these measurements be made accurately. However, the temperatures used in these calculations, total and static temperature, are difficult to measure accurately due to velocity error.

Velocity error is the error in thermocouple measurements that arises due to the interaction between a moving fluid and the surface of the thermocouple. Considering the definitions of static and total temperature will help in explaining velocity error. The static temperature is defined as the temperature sensed by an instrument moving along with the fluid and the total temperature is defined as the temperature of the fluid when it is adiabatically brought to rest. Consider the problem of measuring static temperature. To obtain an accurate reading, the experimenter would have to have a thermocouple moving along at the same velocity and in the same direction as the fluid. This is impractical in turbomachinery applications because of the rotating parts. Static pressure is measured by making a small hole in the wall and reading the pressure through the hole. This method for measuring static pressure is valid because the pressure does not change through the boundary layer in a perpendicular direction to the wall [28]. Placing a thermocouple on the wall similar to making a static pressure tap is not a viable option because of the no-slip condition. The no-slip condition stipulates that the fluid velocity must be zero at the wall surface. Thus, the temperature would be closer to the total temperature since the fluid has been brought to rest. However, the kinetic energy of the fluid is not completely changed into thermal energy because some of the energy is dissipated due to the viscosity of the fluid [26, 28]. The wall conductivity also



transports some of the thermal energy away from the thermocouple. Because of viscosity and conductivity, the thermocouple will read a temperature between the static and total temperature. This demonstrates the difficulty in measuring static temperature.

Measuring the total temperature is easier than measuring the static temperature. The same issue of viscous dissipation is encountered when inserting a thermocouple into a moving fluid since the velocity of the fluid must be zero on the surface of the thermocouple. However, a total temperature probe can be used, which is designed to bring the fluid adiabatically to rest by placing a shroud just barely downstream of a thermocouple. Some total temperature probes are quite complicated. These probes are commonly used in larger turbomachinery test stands. However, these total temperature probes are both larger and more expensive than un-shrouded thermocouples. For smaller research stands where there are space and money limitations, total temperature probes may be impractical. Just inserting a thermocouple into the flow provides an easy and inexpensive means to measure the temperature. Several turbomachinery researchers have opted for this method [6, 12, 14, 18, 25]. In this situation, it is common to simply increase the error of the thermocouple in the error analysis and use an un-shrouded thermocouple. However, the velocity error can be quite large and was found to be up to 10°C in the current research.

Applying a recovery factor to the thermocouple junction temperature corrects the measured temperature to the actual total temperature of the moving fluid and significantly decreases the velocity error. The recovery factor is a measure of how much of the kinetic energy of the fluid was converted to thermal energy on the surface of the thermocouple. Paniagua *et al.* [29] experimentally determined the recovery factor for wire thermocouples with wire diameters of 25 to 90  $\mu\text{m}$  using a method similar to the one presented in this paper. However, recovery factor data for sheathed thermocouples or other thermocouple sizes was not available.

This appendix will begin with a discussion of the test apparatus and the measurements taken. The experimentally determined recovery factor will then be presented and compared with previous research. The recovery factor will be used to correct two different data sets to demonstrate capability. Knowing the recovery factor will help researchers using smaller turbomachinery to make better performance measurements. It will also benefit researchers

who are using these thermocouples to measure flow temperature in any compressible flow situation.

## B.2 Methods

### B.2.1 Jet Production

Determining the recovery factor of a thermocouple requires moving air with known velocity and total properties. In the current study this was accomplished using a TSI 1127 Air Velocity Calibrator shown in Figure B.1. This device is normally used to calibrate hot wire anemometry probes, and was selected because it can produce an air jet with a Mach number of 0 to 1.



Figure B.1: TSI 1127 Air Velocity Calibrator.

The calibrator operates on the principles of compressible flow theory. Compressed air is supplied to a plenum and then passes through a converging nozzle. In the current case, a 6 mm diameter nozzle was used. The velocity inside the plenum can be approximated as zero because of the large area in relation to the nozzle. Thus, temperature and pressure measurements in the plenum can be assumed to be the stagnation quantities. The nozzle exit Mach number and velocity can be calculated using basic compressible flow theory shown in Equations B.1 and B.2. The static pressure of the jet at the exit will be atmospheric pressure [28].

$$M = \sqrt{\frac{2}{\gamma - 1} \left[ \left( \frac{p_0}{p} \right)^{(\gamma-1)/\gamma} - 1 \right]} \quad (\text{B.1})$$

$$u = M\sqrt{\gamma RT} \quad (\text{B.2})$$

### B.2.2 Measurements

The thermocouples used in testing were purchased from Omega and were all Type T with a  $1/16$  inch diameter sheath and had an error of  $1^\circ\text{C}$ . Recovery factors were experimentally determined for two different types of thermocouple junctions, grounded and exposed. These two types of thermocouple junctions are shown in Figure B.2.

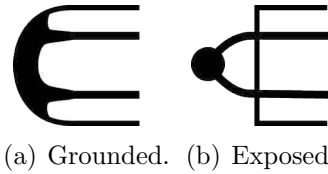
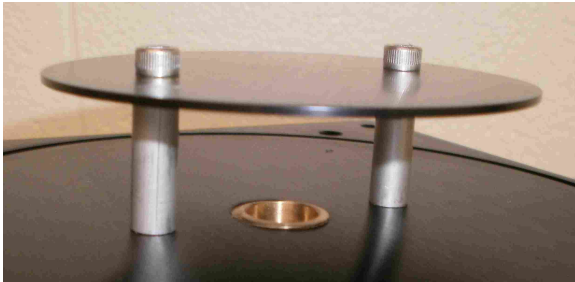


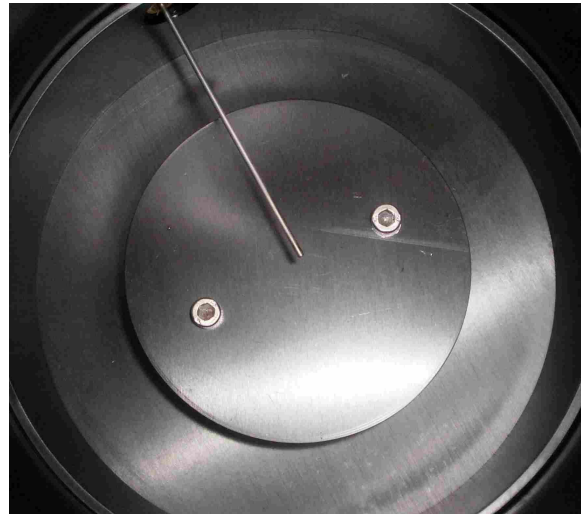
Figure B.2: Diagram of a grounded and an exposed thermocouple.

A grounded thermocouple was positioned inside the plenum to obtain the stagnation temperature of the air before it passed through the nozzle. At the bottom of the plenum there is a plate where the incoming air impinges. This plate serves to slow the incoming air and distribute the air evenly to pressurize the entire plenum. This plate is shown in

Figure B.3(a). Placing the thermocouple tip near the edge of this plate would introduce velocity error into the measurement because of the flow around the plate into the plenum. Thus, the thermocouple tip was placed above and near the center of the plate, where the flow would have the minimum velocity. The placement of the thermocouple is shown in Figure B.3(b). This grounded thermocouple was used for all of the tests and was not changed since it yielded the total temperature of the air and was not affected by velocity error.



(a) Plate.



(b) Thermocouple.

Figure B.3: Thermocouple position above plate.

The thermocouples being tested were placed at the nozzle exit with the tip positioned at the center of the jet approximately 0.75 nozzle diameters above the nozzle exit. Placement of the thermocouple above the nozzle is shown in Figure B.4. The thermocouple needed to be close to the jet exit to minimize jet expansion and heat transfer before the flow impinged on the thermocouple [29]. This thermocouple temperature is referred to in this paper as the nozzle temperature. The atmospheric temperature was measured with a thermocouple placed in stagnate room air.

Pressure measurements were taken with transducers purchased from Omega with a full scale of 50 psia and an error of 0.25% of the full scale value. The total pressure of the velocity jet was measured inside the plenum just upstream of the nozzle. The pressure of the



Figure B.4: Thermocouple position above nozzle.

jet at the exit of a converging nozzle is atmospheric pressure, so the atmospheric pressure was measured to determine the nozzle exit pressure.

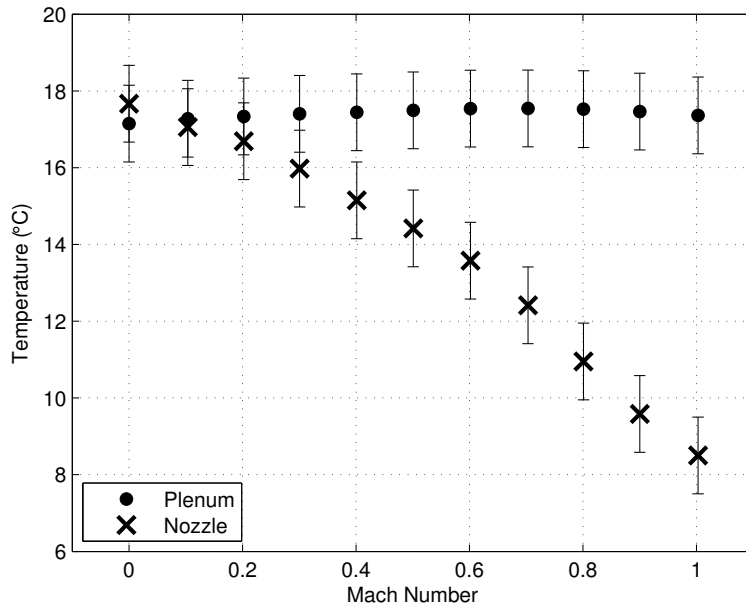
Both the temperature and pressure measurements were connected to a Compaq-RIO device and read with LabVIEW software at a data acquisition rate of 100 Hz.

### **B.2.3 Procedure**

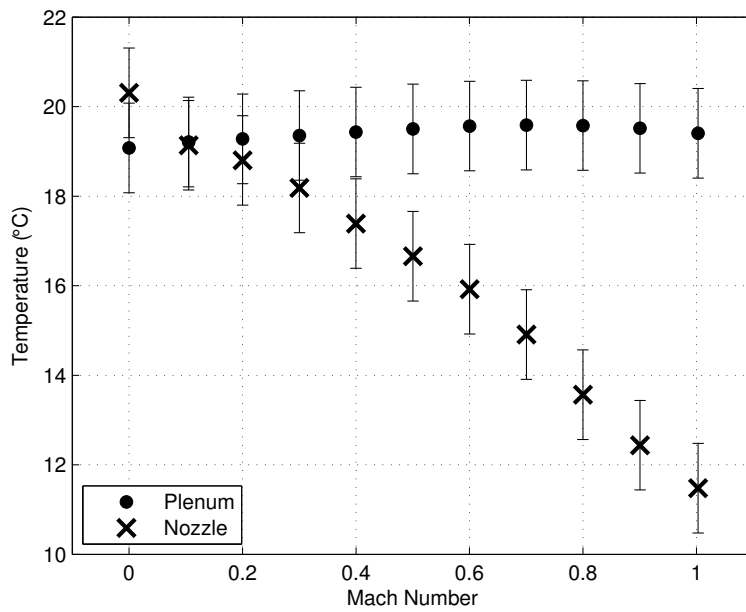
Each thermocouple tested was first positioned above the nozzle exit as previously described. Data sets were taken from Mach 0 to Mach 1 in increments of 0.1. Before taking data at each set-point, the thermocouple was allowed to reach steady state. Steady state was defined when the tens digit of the thermocouple reading was no longer changing. Considering that the thermocouple error is  $1^{\circ}\text{C}$ , this is a good metric since it is an order of magnitude less than the error. Five thermocouples of each junction type were tested.

### **B.3 Results**

The data from all five thermocouples of each junction type were averaged to obtain the results presented below. Measured temperatures for the plenum and nozzle exit are shown in Figure B.5 with error bars of a constant  $1^{\circ}\text{C}$ , since this is the thermocouple error.



(a) Grounded thermocouple.



(b) Exposed thermocouple.

Figure B.5: Mean plenum and nozzle temperatures for both thermocouple junction types with error bars. The error on all temperature measurements is a constant 1°C.

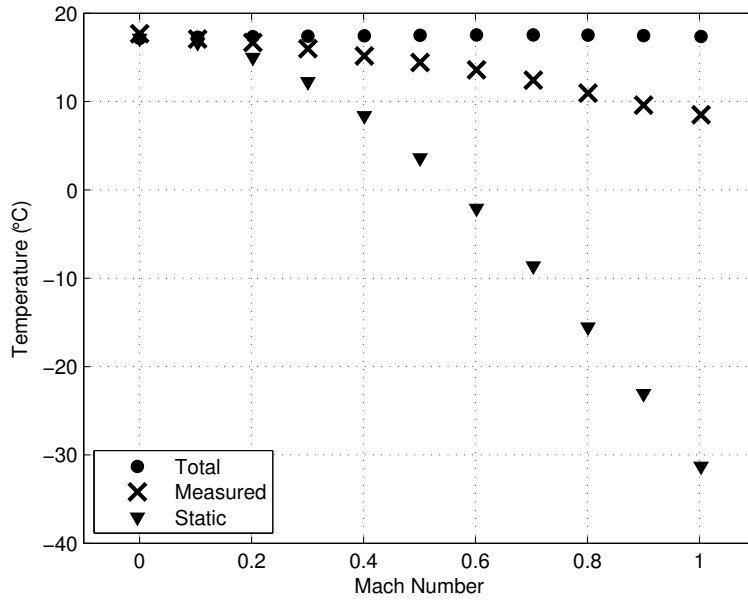
Figure B.6 compares the measured data with the calculated static temperature. This figure visually shows the statement made in Section B.1, that a thermocouple in a flowing fluid will measure a value between the total temperature and static temperature. In compressible flow theory it is generally assumed that the flow is incompressible until a Mach number of 0.3. The plots in Figure B.6 show that the total and static temperatures are about the same until Mach 0.3, where the values start to become drastically different. Also, the total temperature of the air is constant for all Mach numbers. These three factors demonstrate that the results coincide with what would be expected.

The error associated with calculating the Mach number was calculated with a sequential perturbation method presented by Figliola and Beasley [26]. The percent error associated with each Mach number is shown in Figure B.7. Because the same pressure transducers were used for testing both thermocouple junction types, the Mach number percent error curve was the same for all thermocouples tested. The percent error is greater than 10% for Mach numbers less than 0.4. This behavior is not surprising since the pressure transducer error is based on a full scale value. When the pressure difference across the nozzle is low (low Mach numbers), the ratio of pressures used in the calculation of Mach number is more sensitive to this error. However, when the pressure difference across the nozzle is high (high Mach numbers), the pressure ratio will be less sensitive to the error of the transducer.

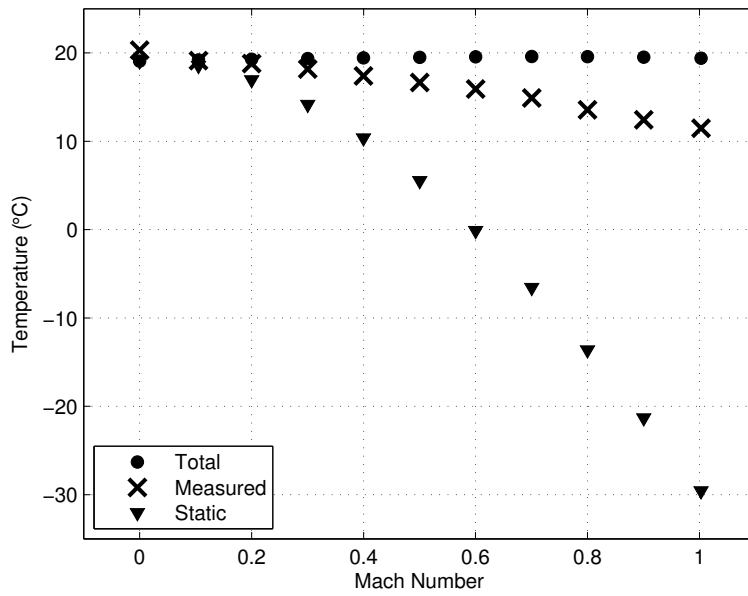
From the above data, the recovery factor for each thermocouple junction type can be calculated. As stated above, the recovery factor is a measure of how much of the kinetic energy was converted to thermal energy on the thermocouple surface. A recovery factor of 1 means that all of the kinetic energy of the flow was converted to thermal energy on the thermocouple surface. The equation to calculate the recovery factor is

$$r = 1 - \frac{T_0 - T_{junction}}{\frac{u^2}{2c_p}} . \quad (B.3)$$

The calculated recovery factor plots for each thermocouple junction type are shown in Figure B.8 with error bars. The recovery factor error was also calculated with the sequential perturbation method [26]. Because the recovery factor is dependent on the velocity of the



(a) Grounded thermocouple.



(b) Exposed thermocouple.

Figure B.6: Mean plenum, nozzle, and static temperatures for both thermocouple junction types.



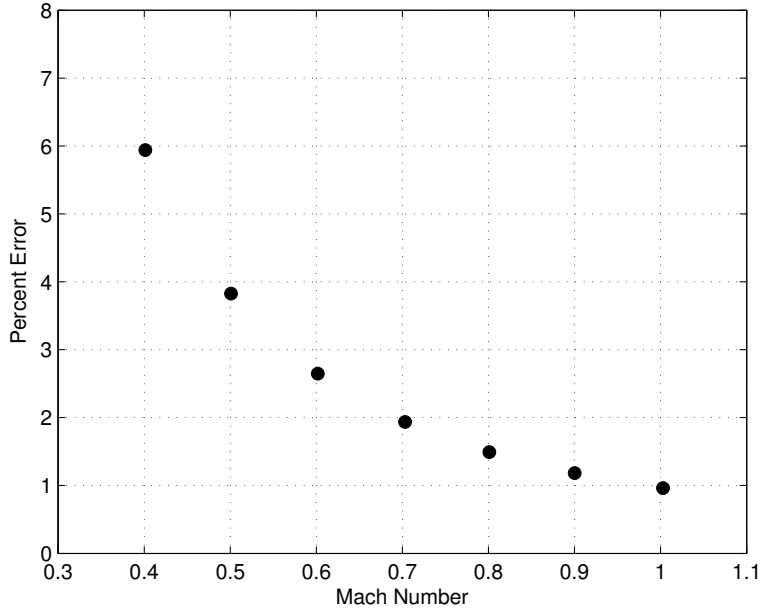


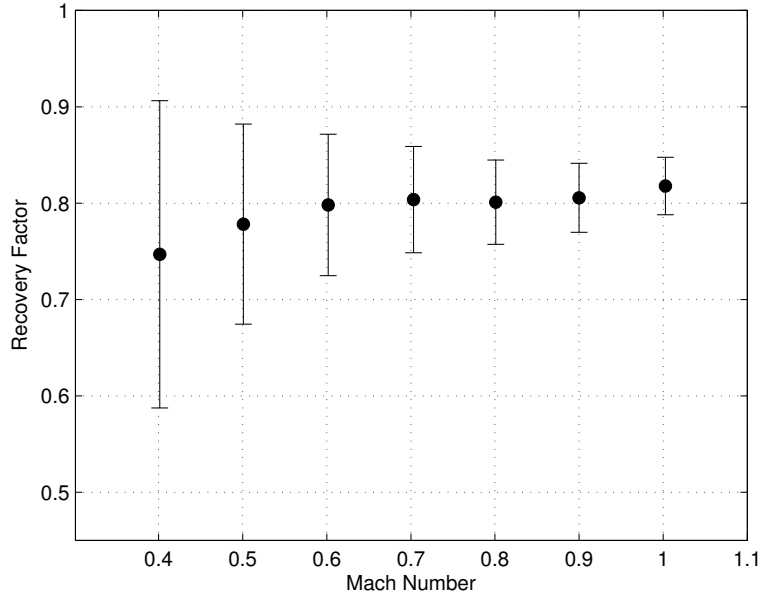
Figure B.7: Calculated Mach number percent error.

flow, the error follows the same trend as the Mach number error. Tabulated values for the recovery factor error are found in Table B.1.

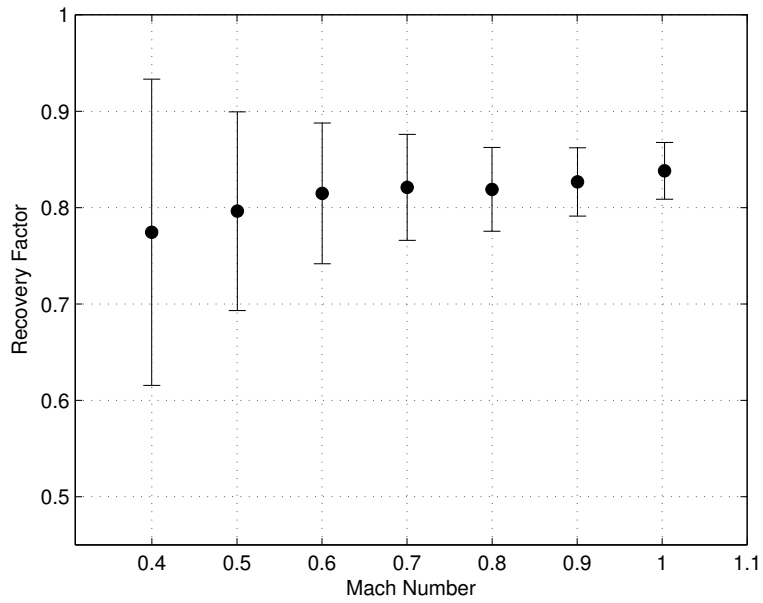
Table B.1: Recovery factor error for grounded and exposed thermocouples.

Mach #	<i>r</i> Error	
	Grounded	Exposed
0.1	2.86	
0.2	0.615	
0.3	0.281	
0.4	0.159	0.159
0.5	0.104	0.103
0.6	0.073	0.073
0.7	0.055	0.055
0.8	0.043	0.044
0.9	0.036	0.035
1.0	0.030	0.030

It is important to note the error bars on the data points in Figure B.8. These error bars are the measurement uncertainty and show that none of the recovery factors are statistically



(a) Grounded thermocouple.



(b) Exposed thermocouple.

Figure B.8: Recovery factor for both types of thermocouples with error bars.

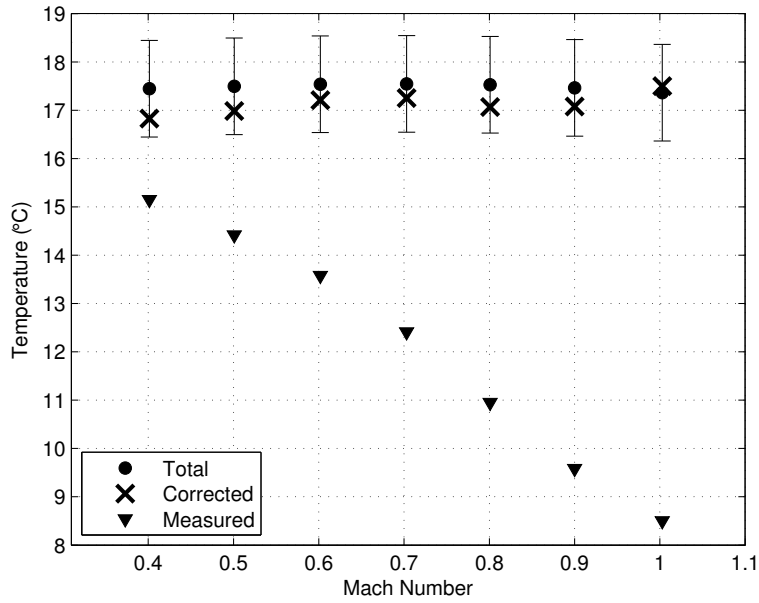
different than the others, both within and between the two junction types. Because of this, it was most appropriate to use an average of the data. The large error values associated with the lower Mach numbers were a concern, so the average was calculated based on data for Mach numbers of 0.6 and above. The recovery factor for  $1/16$  inch sheathed thermocouples was determined to be 0.815.

The recovery factor result of 0.815 compares very well with the results obtained by Paniagua *et al.* [29]. They obtained recovery factors between 0.6 and 0.8 depending on thermocouple size for thermocouples 25 to 90  $\mu\text{m}$  in diameter. In comparison, the data presented in this paper was taken with  $1/16$  inch thermocouples, which are considerably larger. A larger thermocouple diameter means there is more surface on which to recover the kinetic energy of the moving fluid, thus, a higher recovery factor is expected. Considering the result of Paniagua *et al.* also demonstrates that the results of this appendix only apply to  $1/16$  inch sheathed thermocouples because a different sized thermocouple might have a different recovery factor. Another comparison point for the obtained data is the relatively constant recovery factor after about Mach 0.6. Concerning this, Figliola and Beasley [26] state that for Mach numbers greater than 0.1, where the velocity error is significant, the recovery factor tends to be constant. This pattern is also observed in the presented data.

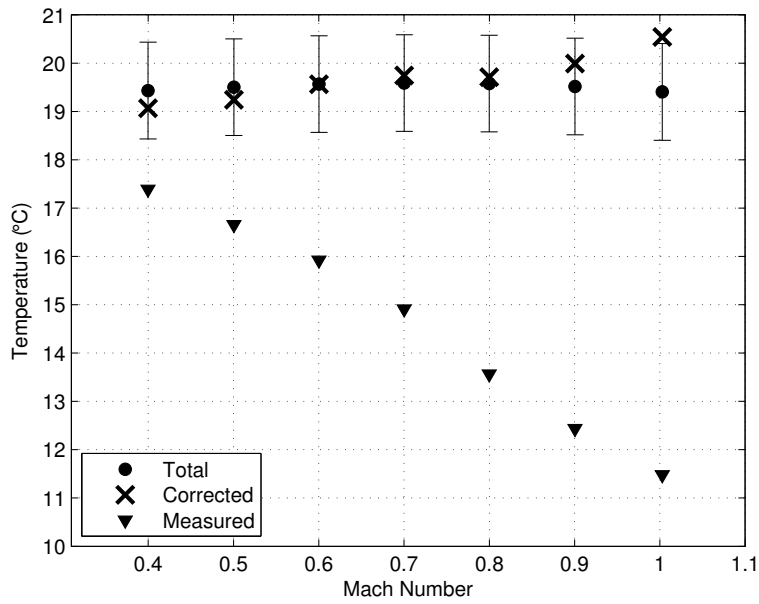
To demonstrate the effect of the recovery factor, the determined value of 0.815 was used to correct the mean measured nozzle temperatures. These results are shown in Figure B.9. Almost all of the corrected temperatures are within the error of the measured total temperature. Due to measurement error, it would be unreasonable to expect all of the corrected values to match well. However, this figure demonstrates that a recovery factor can effectively be used to correct the measured temperatures.

The correction amount at each Mach number is shown in Figure B.10. Notice that for Mach numbers greater than 0.3 the correction amount becomes important because it is greater than the thermocouple error of  $1^\circ\text{C}$ . Again, this is in agreement with compressible flow theory. These plots show that as the Mach number increases, applying a recovery factor to the temperature measurement becomes more important.

Another important thing to note is the correction amount error. This error was calculated using the lowest  $r$  and highest  $r$  based on the uncertainty of the recovery factor.

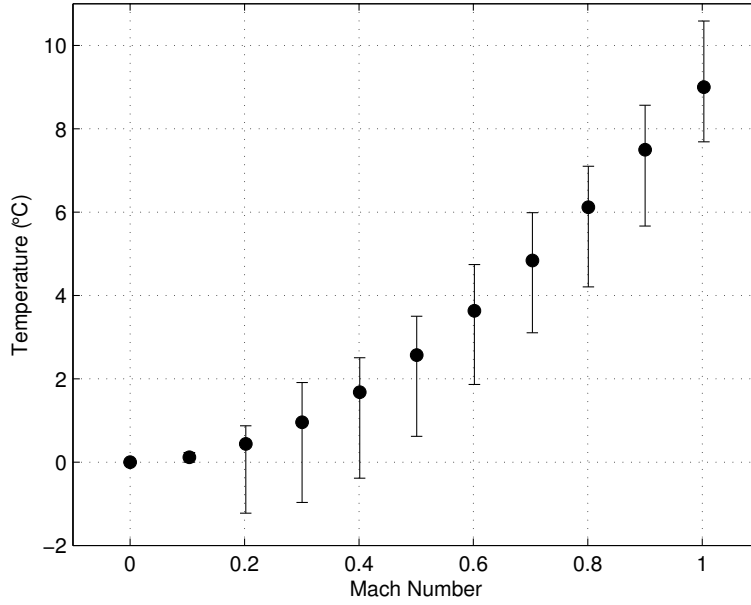


(a) Grounded thermocouple.

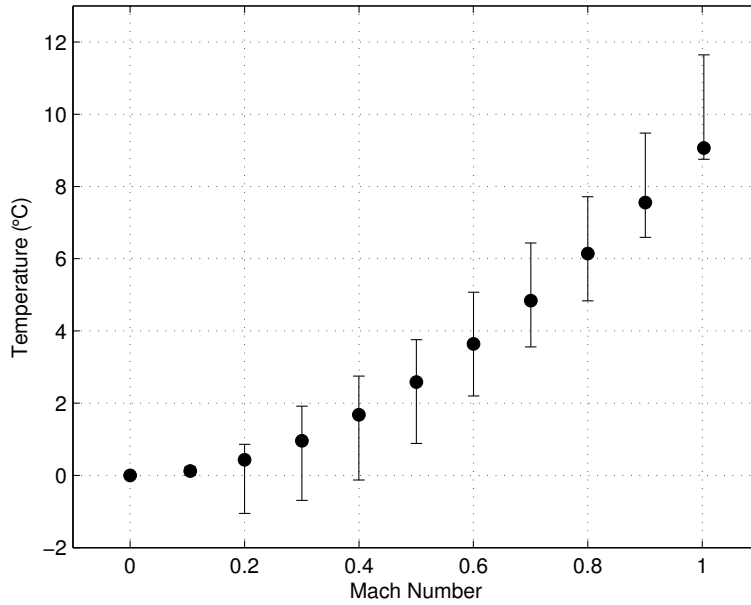


(b) Exposed thermocouple.

Figure B.9: Plenum, nozzle, and corrected temperatures for both types of thermocouples. The error bars are on the plenum temperatures.



(a) Grounded thermocouple.



(b) Exposed thermocouple.

Figure B.10: Amount of correction for both types of thermocouples. The data points are calculated with a recovery factor of 0.815. The error bars represent the uncertainty in the amount of correction and are based on the recovery factor error shown in Table B.1. There is no error for Mach 0 and the error for Mach 0.1 is as large as the data point.

The data points are all calculated using a recovery factor of 0.815. The length of all the error bars above Mach 0.2 is about 3°C. This means that after applying a recovery factor, the thermocouple error will be  $\pm 1.5^\circ\text{C}$ . This result is significant because despite the large error in the thermocouple recovery factor, the error in the amount of correction is constant for compressible velocities. While not eliminating the velocity error, it does dramatically decrease the error.

The presented recovery factor data is very useful to researchers performing flow temperature measurements with an un-shrouded thermocouple inserted into the flow. Information about the recovery factor will allow them to correct the measured values to more closely reflect the true total temperature and decrease the error of their measurements.

#### **B.4 Conclusions**

Un-shrouded thermocouples are often used in turbomachinery applications to measure the temperature of the working fluid when there are monetary and space constraints. However, measuring the total temperature of a moving fluid with an un-shrouded thermocouple results in a large error. This error can be significantly reduced by applying a recovery factor to the thermocouple reading to correct it to the actual total temperature.

The recovery factor for grounded and exposed,  $1/16$  inch diameter, Type T, sheathed thermocouples was determined to be 0.815. Applying this recovery factor would decrease the measurement error to  $\pm 1.5^\circ\text{C}$ . These results compare well with previous research and what would be expected based on compressible flow theory. Also, recovery factor can successfully be used to correct measured temperatures.

## APPENDIX C. TESTING PROCEDURES

### C.1 System Checks

1. Ensure compressor exit piping is pointed in a safe direction and secured
2. Check that all downstream valves are open
3. Check turbine alignment
4. Run lubrication system while spinning compressor so that about 10 mL of oil is pushed into the turbine. After a little wait this should cause oil to come out the nozzle of the turbine.
5. Ensure oil absorption pad is secured underneath turbine
6. Fill lubrication system
7. Make sure all safety shields are properly installed
8. Ensure all sensors are connected properly
9. Verify the LabVIEW program is operational and all sensors give reasonable values
10. Record barometric pressure in the LabVIEW program
11. Zero pressure readings in the LabVIEW program
12. Open doors to test cell
13. Set the compressor to vary between 140 and 150 psi
14. Make sure pressure readings are still zeroed
15. Make sure everyone is out of the test cell

16. Unlock the valve from the air compressor
17. Put caution sign chair out.
18. Turn on exhaust vent in test room.

## **C.2 To do Every Run**

1. Recharge compressor
2. Spin the compressor to see if there are any strange noises
3. Label the file as the appropriate setpoint
4. Check and record the atmospheric pressure
5. Turn on oil flow
6. Begin recording data
7. Start airflow
8. Turn off airflow after 30 sec (30 sec is the time necessary for the compressor exit temperature to reach steady state)

## **C.3 Shut-down Procedures**

1. Spin compressor and check for funny noises
2. Turn off power for the motor
3. Reset compressor to vary between 120 and 150 psi and shut it down if applicable
4. Remove the chair
5. Lock the valve
6. Turn off exhaust vent
7. Move files onto J drive



## APPENDIX D. SEQUENTIAL PERTURBATION ERROR ANALYSIS

This method is from the textbook by Figliola and Beasley [26]. First, the desired value,  $R_0$ , is calculated based on the measured parameters.

$$R_0 = f(x_1, x_2, \dots, x_L) \quad (\text{D.1})$$

The measured values are then perturbed by their uncertainty and the resulting  $R$  is calculated.

$$\begin{aligned} R_1^+ &= f(x_1 + u_{x_1}, x_2, \dots, x_L) \\ R_2^+ &= f(x_1, x_2 + u_{x_2}, \dots, x_L) \\ &\vdots \\ R_L^+ &= f(x_1, x_2, \dots, x_L + u_{x_L}) \end{aligned} \quad (\text{D.2})$$

The values for  $R_i^-$  are calculated using a similar method. The differences between the solutions are then calculated using

$$\begin{aligned} \delta R_i^+ &= R_i^+ - R_0 \\ \delta R_i^- &= R_i^- - R_0 \end{aligned} \quad (\text{D.3})$$

The average error is calculated

$$\delta R_i = \frac{\delta R_i^+ - \delta R_i^-}{2} \quad (\text{D.4})$$

The uncertainty associated with  $R$  can then be calculated with a root sum of the squares

$$u_R = \pm \left[ \sum_{i=1}^L (\delta R_i)^2 \right]^{1/2} \quad (\text{D.5})$$